Journal of
Mechanics of
Materials and Structures

Xiao-Wei Jiang and Hai Wang

msp

■msp

ORDINARY STATE-BASED PERIDYNAMICS
FOR OPEN-HOLE TENSILE STRENGTH PREDICTION
OF FIBER-REINFORCED COMPOSITE LAMINATES

XIAO-WEI JIANG AND HAI WANG

This study presents an ordinary state-based peridynamic model (OSB PD) for open-hole tensile strength prediction of fiber-reinforced composite laminates. The transverse Poisson's effect of composites is considered in the present OSB PD composite model, ensuring a precise capture of typical damage patterns and failure modes of composite laminates, especially when capturing the effect of thickness on damage patterns. The out-of-plane bond considers not only the adjacent plies, but also all the plies within the spherical horizon. The in-plane mesh could be much larger than the out-of-plane mesh, forming an "uneven spherical horizon". The validation of the present model is demonstrated by several numerical results. Typical damage patterns and failures modes of open-hole composite laminates under tensile loading are illustrated, and the effect of thickness on damage patterns is also discussed.

1. Introduction

Aircraft structures are ideal applications of fiber-reinforced composite laminates, due to their high specific stiffness/strength, low coefficient of thermal expansion, and excellent fatigue resistance [Camanho and Lambert 2006]. For the design of composite structures, open-hole tensile strength is a fundamental datum for structural design allowables [ASTM 2011]. In the building block approach for designing composite structures, testing and analysis are both needed due to the overall consideration of cost and reliability [US-DoD 2002]. Conventional analysis methods, normally the finite element method (FEM), have been widely used in open-hole tensile strength predictions of fiber-reinforced composite laminates [Camanho et al. 2007; Hallett et al. 2009; Chen et al. 2013; Aidi and Case 2015; Su et al. 2015; Bao and Liu 2016; Bartan et al. 2016; Moure et al. 2016; Mohammadi et al. 2017]. However, as stated in [Askari et al. 2006; Xu et al. 2008; Kilic et al. 2009; Oterkus and Madenci 2012a; 2012b; Hu et al. 2015; Diyaroglu et al. 2016; Hu and Madenci 2016; Sun and Huang 2016; Yu et al. 2016], conventional analysis methods based on classical continuum mechanics require that the displacement field of the body should be continuously differential for the spatial displacement derivatives of partial differential equations; this requirement contradicts the inherent discontinuity that exists in fracture and damage. Besides, conventional analysis methods, including FEM, usually need a preset damage path, which might not be available for complex loading conditions.

As an alternative to conventional analysis methods, the peridynamic (PD) theory of solid mechanics, which attempts to unite the mathematical modeling of continuous media, cracks, and particles within a single framework, was introduced [Silling 2000; Silling et al. 2007; Silling and Lehoucq 2010]. Peridynamic theory replaces the partial differential equation of the classical theory of solid mechanics with

integral or integral-differential equations, and "spontaneous" formation of fracture and damage could be simulated without any prior knowledge of damage path. These two features suggest great potential advantages of PD in the analysis of composite structures. Matrix cracking, fiber breakage, and delamination: these typical damage modes of composites could bring about severe discontinuities in structures during the loading process. Besides, in most cases, a preset for the damage path of these damage modes is impossible or leads to a huge expense. For example, in order to precisely capture the delamination damage of composite laminates based on FEM, a cohesive zone element (CZE) has to be preset between each adjacent ply, which could result in huge computation cost and convergence problems.

The application of the peridynamic theory into the analysis of composite structures is emerging. Askari et al. [2006] analyzed the damage and failure of composite panels under static and dynamics loads. Xu et al. [2007; 2008] predicted in detail the delamination and matrix damage process in composite laminates under biaxial loads and low-velocity impact. Kilic et al. [2009] predicted the damage in center-cracked laminates with different fiber orientations. Oterkus et al. [2010] present an approach based on the merger of classical continuum theory and peridynamic theory to predict failure simulations in bolted composite lap joints. Hu et al. [2011; 2012] proposed a homogenization-based peridynamic model for simulating fracture and damage in fiber-reinforced composites, and analyzed the dynamic effects induced by different types of dynamic loading. Oterkus and Madenci [2012a; 2012b] present an application of PD theory in the analysis of fiber-reinforced composite materials subjected to mechanical and thermal loading conditions. Damage growth patterns of preexisting cracks in fiber-reinforced composite laminates subjected to tensile loading were computed. Oterkus et al. [2012] present an analysis approach based on a merger of the finite element method and the peridynamic theory. The validity of the approach is established through qualitative and quantitative comparisons against the test results for a stiffened composite curved panel with a central slot under combined internal pressure and axial tension. Hu et al. [2014] developed a PD composite model that accounts for the variation of bond *micromodulus* based on the angle between the bond direction and fiber orientation. As an extension of this model, Hu et al. [2015] developed an energy-based approach to simulate delamination under different fracture mode conditions. Furthermore, Hu and Madenci [2016] present a new bond-based peridynamic modeling of composite laminates without any limitation to specific fiber orientation and material properties in order to consider arbitrary laminate layups. Sun and Huang [2016] proposed a peridynamic rate-dependent constitutive equation and a new interlayer bond describing interlayer interactions of fiber-reinforced composite laminates.

The above peridynamic models for the analysis of composite structures are bond-based peridynamics. Comparatively, ordinary state-based (OSB) peridynamic models for the analysis of composite structures are quite few. Colavito, Madenci, and Oterkus [Colavito 2013; Colavito and Barut 2013; Madenci and Oterkus 2014] presented an OSB peridynamic laminate theory (PDLT) for composite structures. This OSB PDLT was used by Hu et al. [2016] for progressive damage predictions in open-hole quasi-isotropic laminates under tension and compression, and by Diyaroglu et al. [2016] to predict nonlinear transient deformation and damage behavior of composites under shock or blast types of loadings due to explosions. However, the transverse Poisson's effect is neglected in this OSB PDLT model. The out-of-plane horizon of this OSB PDLT model considers only the adjacent layers, and two different types of out-of-plane bonds, the normal bonds and the shear bonds, are introduced in this OSB PDLT model. For a symmetric-layup composite laminate under in-plane tensile loading, which has no coupling between bending and extension, the out-of-plane deformation caused by transverse Poisson's ratio ν_{13} and ν_{23} is neglected

by this OSB PDLT model. This neglect might make this OSB PDLT model insensitive to the effect of thickness on damage patterns of composite laminates, especially for delamination damage.

In the present paper, we are trying to present an ordinary state-based peridynamic (OSB PD) composite model for the open-hole tensile strength prediction of fiber-reinforced composite laminates that considers the transverse Poisson's effect of composites. A spherical horizon, instead of the adjacent-layer horizon in the previous OSB PDLT model, for out-of-plane bonds is used. The out-of-plane normal bond and shear bond in the previous OSB PDLT model are also abandoned. The deformation caused by transverse Poisson's ratios ν_{13} and ν_{23} of composites is taken into account in the present OSB PD composite model, ensuring a precise capture of typical damage patterns and failure modes of composite laminates, especially when capturing the effect of thickness on damage patterns. Although each ply has to be meshed, the in-plane mesh could be much larger than the out-of-plane mesh, forming an "uneven spherical horizon". The validation of the present model is demonstrated by several numerical results. Typical damage patterns and failures modes of open-hole composite laminates under tensile loading are illustrated, and the effect of thickness on damage patterns is also discussed. The numerical analysis is carried out via PGI CUDA FORTRAN compiler (GPU-parallel computing), on the P100 cluster node at the High Performance Computing Center (HPCC) of Shanghai Jiao Tong University.

2. Ordinary state-based peridynamic model for composite laminates

2.1. *Governing equation.* Starting from the work done by Colavito, Madenci and Oterkus [Colavito 2013; Colavito and Barut 2013; Madenci and Oterkus 2014], the governing equation of the present ordinary state-based (OSB PD) peridynamic model for composite laminates can be expressed by

$$\rho_{(k)}^{(n)} \ddot{\boldsymbol{u}}_{(k)}^{(n)} = \sum_{j=1}^{\infty} [\boldsymbol{t}_{(k)(j)} - \boldsymbol{t}_{(j)(k)}] V_{(j)} + \boldsymbol{b}_{(k)}^{(n)}, \tag{1}$$

where $\rho_{(k)}^{(n)}$ is the density of material point $\boldsymbol{x}_{(k)}^{(n)}$, $\ddot{\boldsymbol{u}}_{(k)}^{(n)}$ is instantaneous acceleration of $\boldsymbol{x}_{(k)}^{(n)}$, and n denotes the layer number of laminates, as shown in Figure 1. Furthermore, $\boldsymbol{b}_{(k)}^{(n)}$ is the external load density; $\boldsymbol{t}_{(k)(j)}$ and $\boldsymbol{t}_{(j)(k)}$ are the PD force densities between $\boldsymbol{x}_{(k)}^{(n)}$ and $\boldsymbol{x}_{(j)}$, where $\boldsymbol{x}_{(j)}$ includes both in-plane material points and out-of-plane material points. The PD force density can be expressed as

$$\boldsymbol{t}_{(k)(j)} = A_{(k)(j)} \frac{\boldsymbol{y}_{(j)} - \boldsymbol{y}_{(k)}^{(n)}}{|\boldsymbol{y}_{(j)} - \boldsymbol{y}_{(k)}^{(n)}|}, \tag{2}$$

$$\boldsymbol{t}_{(j)(k)} = B_{(j)(k)} \frac{\boldsymbol{y}_{(k)}^{(n)} - \boldsymbol{y}_{(j)}}{|\boldsymbol{y}_{(k)}^{(n)} - \boldsymbol{y}_{(j)}|}, \tag{3}$$

with

$$A_{(k)(j)} = 2ad \frac{\delta}{|\boldsymbol{x}_{(j)} - \boldsymbol{x}_{(k)}^{(n)}|} \Lambda_{(k)(j)} \theta_{(k)} + 2\delta b s_{(k)(j)} + 2\delta(\mu_F b_F + \mu_T b_T) s_{(k)(j)}^{(n)(n)}, \tag{4}$$

$$B_{(j)(k)} = 2ad \frac{\delta}{|\boldsymbol{x}_{(k)}^{(n)} - \boldsymbol{x}_{(j)}|} \Lambda_{(k)(j)} \theta_{(j)} + 2\delta b s_{(j)(k)} + 2\delta(\mu_F b_F + \mu_T b_T) s_{(j)(k)}^{(n)(n)}, \tag{5}$$
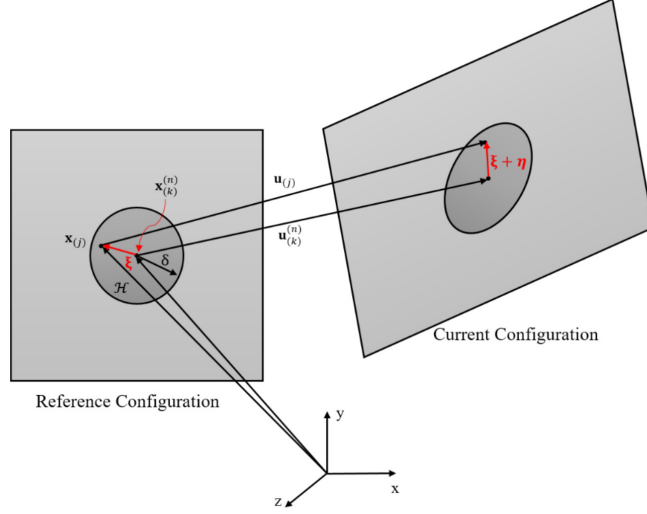
Figure 1. Peridynamic notations.

and

$$s_{(k)(j)} = \frac{|\boldsymbol{y}_{(j)} - \boldsymbol{y}_{(k)}^{(n)}| - |\boldsymbol{x}_{(j)} - \boldsymbol{x}_{(k)}^{(n)}|}{|\boldsymbol{x}_{(j)} - \boldsymbol{x}_{(k)}^{(n)}|}, \tag{6}$$

$$s_{(k)(j)}^{(n)(n)} = \frac{|\boldsymbol{y}_{(j)}^{(n)} - \boldsymbol{y}_{(k)}^{(n)}| - |\boldsymbol{x}_{(j)}^{(n)} - \boldsymbol{x}_{(k)}^{(n)}|}{|\boldsymbol{x}_{(j)}^{(n)} - \boldsymbol{x}_{(k)}^{(n)}|}, \tag{7}$$

and

$$\mu_F = \begin{cases} 1 & (\boldsymbol{x}_{(j)}^{(n)} - \boldsymbol{x}_{(k)}^{(n)}) \| \text{ fiber direction,} \\ 0 & \text{otherwise,} \end{cases} \tag{8}$$

$$\mu_T = \begin{cases} 1 & (\boldsymbol{x}_{(j)}^{(n)} - \boldsymbol{x}_{(k)}^{(n)}) \perp \text{ fiber direction,} \\ 0 & \text{otherwise,} \end{cases} \tag{9}$$

where $s_{(k)(j)}$ is the stretch of bonds, $s_{(k)(j)}^{(n)(n)}$ denotes the in-plane fiber direction bond stretch. In (4) and (5), δ is the radius of the horizon zone. The direction cosines of the relative position vectors between the material points $\boldsymbol{x}_{(k)}^{(n)}$ and $\boldsymbol{x}_{(j)}$ in the undeformed and deformed states are defined as

$$\Lambda_{(k)(j)} = \frac{\boldsymbol{y}_{(j)} - \boldsymbol{y}_{(k)}^{(n)}}{|\boldsymbol{y}_{(j)} - \boldsymbol{y}_{(k)}^{(n)}|} \cdot \frac{\boldsymbol{x}_{(j)} - \boldsymbol{x}_{(k)}^{(n)}}{|\boldsymbol{x}_{(j)} - \boldsymbol{x}_{(k)}^{(n)}|}. \tag{10}$$

The three-dimensional PD dilatation $\theta_{(k)}$ can be expressed as

$$\theta_{(k)} = d \sum_{j=1}^{\infty} \delta s_{(k)(j)} \Lambda_{(k)(j)} V_{(j)}. \tag{11}$$

The PD material parameters a, d characterize the effect of dilation, and b, b_F, b_T are associated with the deformation of material points in arbitrary directions (in-plane fiber direction and in-plane transverse

direction, respectively). These parameters are related to material properties of composite laminates, horizon radius, and ply direction. The main derivation procedures to get these PD material parameters are illustrated in Section 2.2, and the detailed derivation process will be given in the Appendix. Here we directly give the derived results as

$$a = \tfrac{1}{2}(C_{33} - 3C_{55}), \tag{12}$$

$$d = \frac{9}{4\pi\delta^4}, \tag{13}$$

$$b = \frac{15C_{55}}{2\pi\delta^5}, \tag{14}$$

$$b_F = \frac{C_{11} - C_{33}}{2\delta \sum_{j=1}^{J} |\boldsymbol{x}_{(j)}^{(n)} - \boldsymbol{x}_{(k)}^{(n)}| V_{(j)}^{(n)}}, \tag{15}$$

$$b_T = \frac{C_{22} - C_{33}}{2\delta \sum_{j=1}^{J} |\boldsymbol{x}_{(j)}^{(n)} - \boldsymbol{x}_{(k)}^{(n)}| V_{(j)}^{(n)}}, \tag{16}$$

where C_{11}, C_{22}, C_{33}, and C_{55} are coefficients of composite material stiffness matrix $\boldsymbol{C}$, and are defined as

$$C_{11} = \frac{1 - \nu_{23}\nu_{32}}{E_2 E_3 \Delta}, \quad C_{22} = \frac{1 - \nu_{13}\nu_{31}}{E_1 E_3 \Delta}, \quad C_{33} = \frac{1 - \nu_{12}\nu_{21}}{E_1 E_2 \Delta}, \quad C_{55} = G_{31}, \tag{17}$$

$$\Delta = \frac{1 - \nu_{12}\nu_{21} - \nu_{23}\nu_{32} - \nu_{13}\nu_{31} - 2\nu_{21}\nu_{32}\nu_{13}}{E_1 E_2 E_3}. \tag{18}$$

It may be worth noting that the present OSB PD composite model differs from the OSB PDLT model by using a spherical horizon for out-of-plane bonds, and the transverse Poisson's effect is taken into account, as shown in the parameters in (12)–(18).

2.2. *Derivation of PD material parameters.*
Derivation of the PD material parameters for the present OSB PD composite model follows a similar procedure for deriving the OSB PDLT model presented by Colavito, Madenci, and Oterkus [Colavito 2013; Colavito and Barut 2013; Madenci and Oterkus 2014]. Nevertheless, it might be worth noting that as the normal bond and shear bond in the OSB PDLT model are abandoned in the present OSB PD composite model, the out-of-plane spherical horizon is used and transverse Poisson's effect is considered, so the derivation involving out-of-plane bonds shall be different from OSB PDLT's derivation process.

The PD strain energy density of the present OSB PD composite model for composite laminates can be expressed as

$$W_{(k)}^{(n)} = a\theta_{(k)}^2 + b\sum_{j=1}^{\infty}\delta|\boldsymbol{x}_{(j)} - \boldsymbol{x}_{(k)}|s_{(k)(j)}^2 V_{(j)}$$
$$+ b_F \sum_{j=1}^{J}\delta|\boldsymbol{x}_{(j)}^{(n)} - \boldsymbol{x}_{(k)}^{(n)}|s_{(k)(j)}^{(n)(n)2} V_{(j)}^{(n)} + b_T \sum_{j=1}^{J}\delta|\boldsymbol{x}_{(j)}^{(n)} - \boldsymbol{x}_{(k)}^{(n)}|s_{(k)(j)}^{(n)(n)2} V_{(j)}^{(n)}. \tag{19}$$

The PD material parameters in (4), (5), and (14) can be derived by comparing the PD strain energy density and the strain energy density of continuum mechanics under simple loading conditions. In the
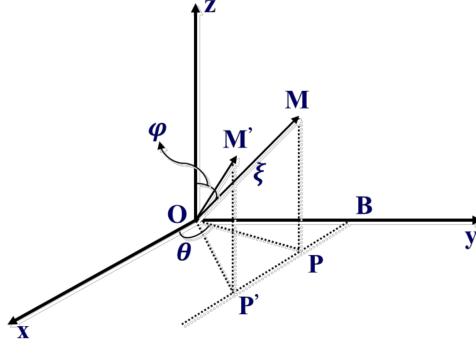
Figure 2. Transverse pure shear loading on xz-plane (γ_{13}).

present model, we derive these parameters by assuming a unidirectional composite laminate under four simple loading conditions:

(1) transverse pure shear loading on xz-plane (γ_{13});

(2) transverse tensile loading (ε_{33});

(3) in-plane uniaxial tension in x direction (ε_{11});

(4) in-plane uniaxial tension in y direction (ε_{22}).

Here we only show the main derivation procedure, and the detailed derivation processes are presented in the Appendix.

2.2.1. *Transverse pure shear loading on xz-plane* (γ_{13}). Under this loading condition, we assume $\gamma_{13} = \zeta$ and all other strains equal zero. From three-dimensional elasticity of orthotropic composite materials, we get

$$\theta_{(k)}^{CM} = 0, \quad W_{(k)}^{CM} = \tfrac{1}{2}C_{55}\zeta^2. \tag{20}$$

Firstly, the stretch of bonds $s_{(k)(j)}$ in (6) should be calculated under $\gamma_{13} = \zeta$. As shown in Figure 2, under this simple loading condition, material point M moves to M':

$$OM' = \sqrt{OM'^2 + M'P'^2} = \sqrt{OB^2 + BP'^2 + M'P'^2}$$

$$= \sqrt{(\xi \sin \varphi \sin \theta)^2 + (\xi \sin \varphi \cos \theta + \zeta\xi \cos \varphi)^2 + (\xi \cos \varphi)^2}$$

$$= \sqrt{\xi^2 + 2\xi \sin \varphi \cos \theta \, \zeta\xi \cos \varphi + (\zeta\xi \cos \varphi)^2}$$

$$\approx \sqrt{\xi^2 + 2\xi \sin \varphi \cos \theta \, \zeta\xi \cos \varphi}. \tag{21}$$

$$s_{(k)(j)} = \frac{OM' - OM}{OM} = \frac{\sqrt{\xi^2 + 2\xi \sin \varphi \cos \theta \, \zeta\xi \cos \varphi} - \xi}{\xi} = \sqrt{1 + \zeta 2 \sin \varphi \cos \theta \cos \varphi} - 1$$

$$\approx 1 + \tfrac{1}{2}\zeta 2 \sin \varphi \cos \theta \cos \varphi - 1 = \zeta \sin \varphi \cos \varphi \cos \theta. \tag{22}$$

Then the PD strain energy can be derived as

$$W_{(k)}^{(n)} = a\theta_{(k)}^2 + b\sum_{j=1}^{\infty} \delta|\boldsymbol{x}_{(j)} - \boldsymbol{x}_{(k)}|s_{(k)(j)}^2 V_{(j)} + b_F \sum_{j=1}^{J} \delta|\boldsymbol{x}_{(j)}^{(n)} - \boldsymbol{x}_{(k)}^{(n)}|s_{(k)(j)}^{(n)(n)2} V_{(j)}^{(n)}$$

$$+ b_T \sum_{j=1}^{J} \delta|\boldsymbol{x}_{(j)}^{(n)} - \boldsymbol{x}_{(k)}^{(n)}|s_{(k)(j)}^{(n)(n)2} V_{(j)}^{(n)}$$

$$\tag{23}$$

$$= b\sum_{j=1}^{\infty} \delta|\boldsymbol{x}_{(j)} - \boldsymbol{x}_{(k)}|s_{(k)(j)}^2 V_{(j)} = b\sum_{j=1}^{\infty} \delta\xi(\zeta \sin\varphi \cos\varphi \cos\theta)^2 V_{(j)}$$

$$= \zeta^2 b\delta \int_0^{2\pi}\int_0^{\pi}\int_0^{\delta} \xi \sin^2\varphi \cos^2\varphi \cos^2\theta \, \xi^2 \sin\varphi \, dr \, d\varphi \, d\theta = \zeta^2 b\frac{\pi^2}{15}\delta^5.$$

Comparing with (23), we get

$$b = \frac{1/2\, C_{55}\zeta^2}{\zeta^2\,\pi/15\,\delta^5} = \frac{15C_{55}}{2\pi\,\delta^5}. \tag{24}$$

2.2.2. *Transverse tensile loading* (ε_{33}). Setting $\varepsilon_{33} = \zeta$ and conducting the same procedure in Section 2.2.1, we get

$$\theta_{(k)}^{CM} = \zeta, \quad W_{(k)}^{CM} = \tfrac{1}{2}C_{33}\zeta^2, \tag{25}$$

$$s_{(k)(j)} = \zeta \cos^2\varphi, \tag{26}$$

$$\theta_{(k)} = \zeta d\tfrac{4}{9}\pi\delta^4, \quad W_{(k)}^{(n)} = a\zeta^2 + \zeta^2\tfrac{3}{2}C_{55}. \tag{27}$$

Comparing (28) and (30), we get

$$d = \frac{9}{4\pi\delta^4}, \quad a = \tfrac{1}{2}(C_{33} - 3C_{55}). \tag{28}$$

2.2.3. *In-plane uniaxial tension in x-direction* (ε_{11}). Similarly, setting $\varepsilon_{11} = \zeta$, we get

$$\theta_{(k)}^{CM} = \zeta, \quad W_{(k)}^{CM} = \tfrac{1}{2}C_{11}\zeta^2, \tag{29}$$

$$s_{(k)(j)} = \zeta \sin^2\varphi \cos^2\theta, \tag{30}$$

$$\theta_{(k)} = \zeta d\tfrac{4}{9}\pi\delta^4, \quad W_{(k)}^{(n)} = a\zeta^2 + \zeta^2 b\frac{\pi}{5}\delta^5 + \zeta^2 b_F \delta \sum_{j=1}^{J}|\boldsymbol{x}_{(j)}^{(n)} - \boldsymbol{x}_{(k)}^{(n)}|V_{(j)}^{(n)}. \tag{31}$$

Substituting a and b, and comparing (32) and (34), we get

$$d = \frac{9}{4\pi\delta^4}, \quad b_F = \frac{1/2\,(C_{11} - C_{33})}{\delta \sum_{j=1}^{J}|\boldsymbol{x}_{(j)}^{(n)} - \boldsymbol{x}_{(k)}^{(n)}|V_{(j)}^{(n)}}. \tag{32}$$

2.2.4. *In-plane uniaxial tension in y-direction* (ε_{22}). Similarly, setting $\varepsilon_{22} = \zeta$, we get

$$\theta_{(k)}^{CM} = \zeta, \quad W_{(k)}^{CM} = \tfrac{1}{2}C_{22}\zeta^2, \tag{33}$$

$$s_{(k)(j)} = \zeta \sin^2\varphi \cos^2\theta, \tag{34}$$

$$\theta_{(k)} = \zeta d\tfrac{4}{9}\pi\delta^4, \quad W_{(k)}^{(n)} = a\zeta^2 + \zeta^2 b\frac{\pi}{5}\delta^5 + \zeta^2 b_T \delta \sum_{j=1}^{J}|\boldsymbol{x}_{(j)}^{(n)} - \boldsymbol{x}_{(k)}^{(n)}|V_{(j)}^{(n)}. \tag{35}$$
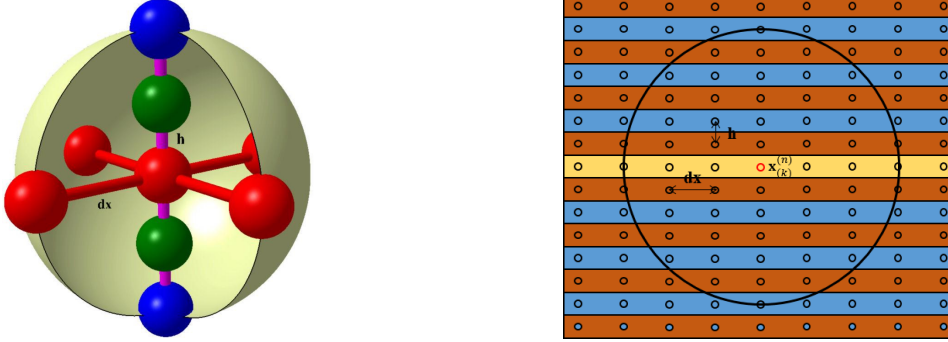
Figure 3. "Uneven spherical horizon" for OSB PD composite model of composite laminates. Left: 3D view, $\delta = \mathrm{d}x$, $\mathrm{d}x = 2h$. Right: 2D view, $\delta = 3\mathrm{d}x$, $\mathrm{d}x = 2h$.

Substituting a and b, and comparing (36) and (39), we can get

$$d = \frac{9}{4\pi\delta^4}, \quad b_T = \frac{1/2\,(C_{22} - C_{33})}{\delta \sum_{j=1}^{J} |\boldsymbol{x}_{(j)}^{(n)} - \boldsymbol{x}_{(k)}^{(n)}| V_{(j)}^{(n)}}. \tag{36}$$

2.3. *Uneven spherical horizon.* The present OSB PD composite model of composite laminates uses a spherical horizon for out-of-plane bonds. The out-of-plane bonds consider not only the adjacent plies, but also all the plies within the spherical horizon. In order to precisely capture the delamination damage between plies of composite laminates, each ply has to be meshed. In the present model, an uneven mesh is adopted for computational efficiency. The in-plane mesh could be much larger than the out-of-plane mesh, forming an "uneven spherical horizon", as shown in Figure 3. The effect of a truncated spherical horizon near the boundaries must be considered. In the present OSB PD composite model, we use the similar surface effect correction procedure as stated in [Madenci and Oterkus 2014], which calculates the surface effect correction factors by comparing the theoretical PD dilatation and strain energy density with numerically discrete PD dilatation and strain energy density under simple loading conditions. For material points which have complete spherical horizon, this correction factor is around 1. For those with a truncated spherical horizon near boundaries, such as top and bottom surfaces of laminates, the correction factor is around 2. By adding these surface effect correction factors into the equation, the surface effect can be significantly reduced.

2.4. *Failure criteria.* The failure criteria used in the present model is similar to other PD models [Hu et al. 2014; 2016]. When the bond stretch between two material points exceeds a critical value, the interaction between these two material points is irreversibly removed. The critical stretches for the in-plane fiber bonds, in-plane matrix bonds, and the remaining arbitrary bonds are shown in Figure 4, and their values can be calculated by

$$\begin{aligned}
s_0^{\mathrm{ft}} &= X^T/E_1, \quad s \geq 0 \quad \text{(fiber bonds)}, \\
s_0^{\mathrm{fc}} &= X^C/E_1, \quad s < 0 \quad \text{(fiber bonds)}, \\
s_0^{\mathrm{mt}} &= Y^T/E_2, \quad s \geq 0 \quad \text{(matrix bonds and arbitrary bonds)}, \\
s_0^{\mathrm{mc}} &= Y^C/E_2, \quad s < 0 \quad \text{(matrix bonds and arbitrary bonds)},
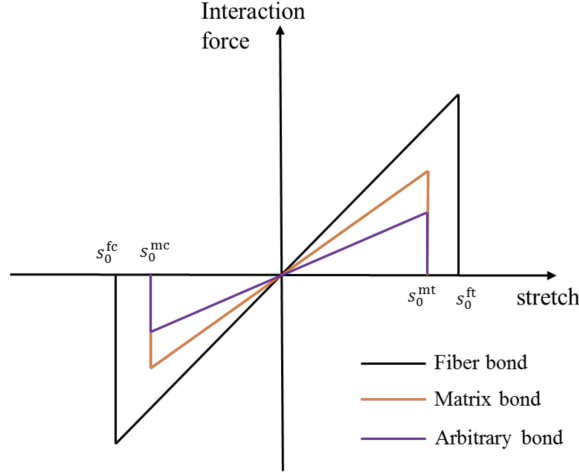\end{aligned} \tag{37}$$

Figure 4. Force-stretch relationships for peridynamic interactions.

where X^T, X^C, Y^T, Y^C are strengths of composite materials.

Local damage at a material point is defined as the weighted ratio of the number of eliminated interactions to the total number of initial interactions of the material point with its family members. The local damage at a point can be quantified as [Silling and Askari 2005; Diyaroglu et al. 2016]

$$\varphi(\boldsymbol{x}, t) = 1 - \frac{\int_H \mu(\boldsymbol{x}' - \boldsymbol{x}, t)\, dV'}{\int_H dV'}. \tag{38}$$

The status variable μ is defined as

$$\mu = \begin{cases} 1 & s < s_c \quad \text{(no damage)}, \\ 0 & s \geq s_c \quad \text{(damage)}. \end{cases} \tag{39}$$

To be specific for the present model, three kinds of typical damage modes of composite laminates can be captured: fiber breakage, in-plane matrix cracking, and delamination. These damage modes are indicated by

$$\varphi_{\text{fiber breakage}} = 1 - \frac{\sum_{j=1}^{J} \mu_{(k)(j)}^{(n)(n)}}{J}, \qquad \varphi_{\text{matrix cracking}} = 1 - \frac{\sum_{j=1}^{N_{(i)}^{(n)}} \mu_{(k)(j)}^{(n)(n)}}{N_{(k)}^{(n)}},$$

$$\varphi_{\text{out-of-plane upper}}^{(n)} = 1 - \frac{\sum_{j=1}^{N_{(k)}^{\text{(upper)}}} \mu_{(k)(j)}^{(n)(n)}}{N_{(k)}^{\text{(upper)}}}, \quad \varphi_{\text{out-of-plane lower}}^{(n+1)} = 1 - \frac{\sum_{j=1}^{N_{(k)}^{\text{(lower)}}} \mu_{(k)(j)}^{(n)(n)}}{N_{(k)}^{\text{(lower)}}}, \tag{40}$$

$$\varphi_{\text{delamination}}^{(n)(n+1)} = \tfrac{1}{2}\left(\varphi_{\text{out-of-plane upper}}^{(n)} + \varphi_{\text{out-of-plane lower}}^{(n+1)}\right),$$

where J is the number of fiber material points inside the horizon, $N_{(k)}^{(n)}$ is the number of in-plane matrix material points inside the horizon, $N_{(k)}^{\text{(upper)}}$ is the number of upper side out-of-plane material points inside the horizon, and $N_{(k)}^{\text{(lower)}}$ is the number of lower side out-of-plane material points inside the horizon.

3. Numerical implementation

Although the peridynamic governing equation is in dynamic form, it can still be used to solve quasistatic or static problems by using the adaptive dynamic relaxation (ADR) method [Kilic and Madenci 2010].

According to the ADR method, (1) at the n-th iteration can be rewritten as

$$\ddot{U}^n(X, t^n) + c^n \dot{U}^n(X, t^n) = D^{-1} F^n(U^n, U'^n, X, X'),$$ (41)

where D is the fictitious diagonal density matrix and c is the damping coefficient, which can be expressed by

$$c^n = 2\sqrt{((U^n)^{T\,1}K^n U^n)/((U^n)^T U^n)},$$ (42)

in which $^1K^n$ is the diagonal "local" stiffness matrix, which is given as

$$^1K_{ii}^n = -(F_i^n/\lambda_{ii} - F_i^{n-1}/\lambda_{ii})/(\Delta t \dot{u}_t^{n-1/2}),$$ (43)

where F_i^n is the value of force vector F^n at material point x, which includes both the peridynamic force state vector and external forces. Here, λ_{ii} is the diagonal elements of D which should be large enough for numerical convergence.

By utilizing central-difference explicit integration, displacements and velocities for the next time step can be obtained:

$$\dot{U}^{n+1/2} = \frac{((2 - c^n \Delta t)\dot{U}^{n-1/2} + 2\Delta t D^{-1} F^n)}{(2 + c^n \Delta t)}$$ (44)

and

$$\dot{U}^{n+1} = U^n + \Delta t \dot{U}^{n+1/2}.$$ (45)

To start the iteration process, we assume that $U^0 \neq 0$ and $\dot{U}^0 = 0$, so the integration can be started by

$$\dot{U}^{1/2} = \frac{\Delta t D^{-1} F^0}{2}.$$ (46)

Due to the large computational cost of the PD model, GPU-parallel computing is introduced. The PGI CUDA FORTRAN compiler, PGI/16.10 Community Edition, is used for compiling. The P100 cluster node at the High Performance Computing Center (HPCC) of Shanghai Jiao Tong University is applied for running the GPU-parallel program. The P100 cluster node has two NVIDIA Tesla P100 graphic cards (3584 CUDA Cores, 16 GB graphic memory), two Intel Xeon E5-2680 CPUs, and 96 GB memory. The GPU block threads are fixed to 256, and the number of blocks depends on the total number of parallel processes [Ruetsch and Fatica 2013].

4. Numerical results

4.1. *Deformation of composite laminated plate.* As shown in Figure 5, a composite laminated plate [45/0/45] under tensile loading is simulated both by the present OSB PD composite model and FEM. The dimensions of the composite laminated plate are $L = 12.5$ mm and $W = 6.25$ mm. The thickness of the plate is 0.375 mm, with 0.125 mm for each ply. The material is the fiber-reinforced composite from [Madenci and Oterkus 2014]. The material properties of the composite are: $\rho = 8000$ kg/m^3, elastic modulus in the fiber direction $E_1 = 159.96$ GPa, elastic modulus in transverse direction $E_2 = 8.96$ GPa,
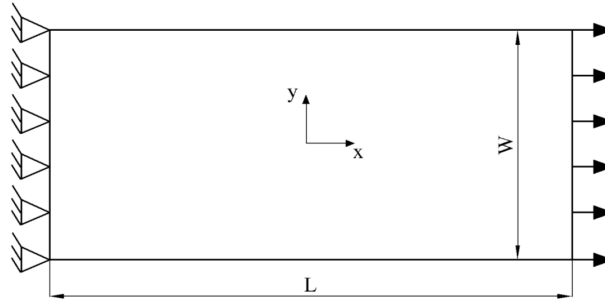
Figure 5. Composite laminated plate [45/0/45] under tensile loading.

in-plane Poisson's ratio $\nu_{12} = 0.33$, and in-plane shear modulus $G_{12} = 3.0054\,\text{GPa}$. The mesh of the PD model is $100 \times 50 \times 3$, with $\text{d}x = h = 0.125\,\text{mm}$, and horizon $\delta = 3\,\text{d}x$.

Under the tensile loading condition, with 0.2 mm displacement at the right end, the deformation of the composite laminated plate is presented in Figure 6. The simulation results of the displacement fields in three directions, U1, U2, and U3, are all compared between PD and FEM. The variation of the in-plane and out-of-plane displacement in the three directions are compared with FEM results in Figure 7. It can be seen from these figures that deformation simulation of the present OSB PD composite model fits the FEM results well. The influence of fiber direction on the displacement fields, especially U2, is precisely captured by the present model. The out-of-plane deformation caused by transverse Poisson's effect is accurately captured by the present OSB PD composite model, as shown in Figure 7, bottom. It should be noted that as FEM and PD use different mesh methods, the calculated points have different coordinates. This is the reason that PD is unable to fit a curved tendency with three mesh points, as seen in Figure 7, bottom. Better results can be seen when a composite laminate with large number plies is simulated, as shown in Figure 12, bottom.

4.2. *Deformation of composite laminated plate with open-hole.* As shown in Figure 8, the deformation of a composite laminated plate with an open-hole is considered. With the same plate dimension, material system, mesh, and loading condition as Section 4.1, the composite laminated plate with an open-hole in this section only has an additional hole with radius $R = 0.5\,\text{mm}$. Similarly, simulation results of displacement fields, U1, U2, and U3, by both PD and FEM are presented in Figure 9. The variation of the in-plane and out-of-plane displacement in the three directions are compared with FEM results in Figure 10. All the deformation results of the present OSB PD composite model fit the FEM results well. The influence of the fiber direction on the displacement field can also be precisely captured. The effect of the hole on the deformation is also obviously observed by comparing Figure 6 and Figure 9. Also, the out-of-plane deformation caused by transverse Poisson's effect is accurately captured by the present OSB PD composite model, as shown in Figure 10, bottom.

In order to illustrate that the present OSB PD composite model is also valid for calculating the deformation of composite laminates with a large number plies, an 8-layer $[90/45/0/-45]_S$ composite laminate with an open-hole is simulated. The dimensions, material system, and loading condition are similar to the case in Figure 8, and only the ply number is changed. The deformation contour is compared with FEM results in Figure 11. The variation of the in-plane and out-of-plane displacement in the three
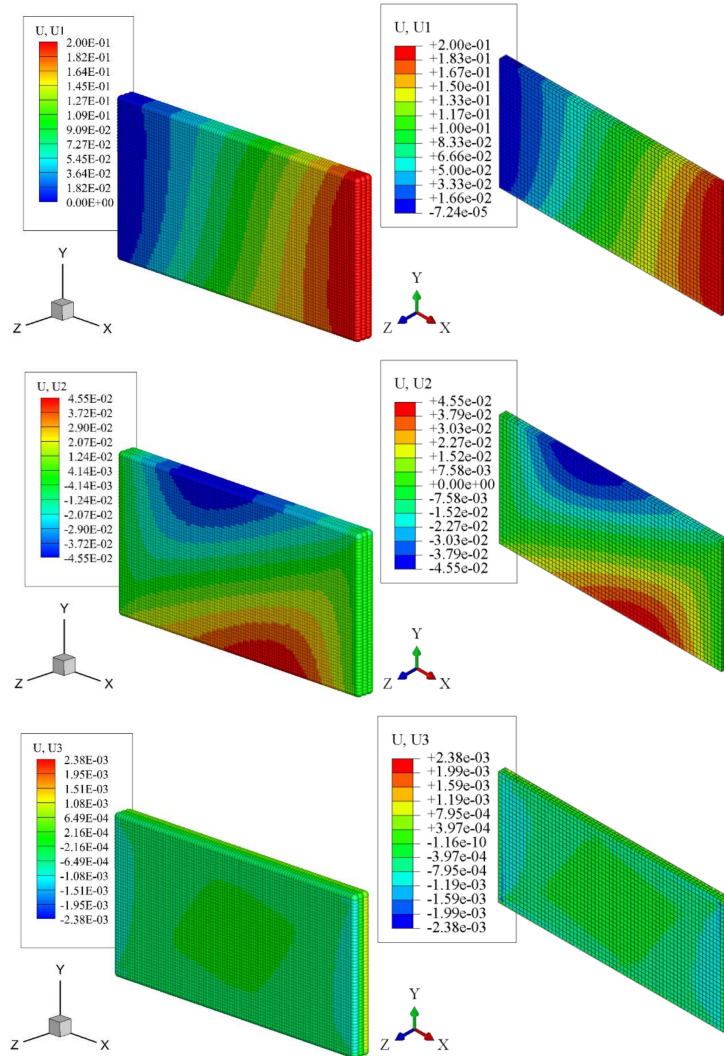
Figure 6. Comparison of the deformation of composite laminated plate [45/0/45] (mm).
Left: PD. Right: FEM.

directions are compared with FEM results in Figure 12. It can be seen from these figures that the calculated deformation results by the present OSB PD composite model fit the FEM results well. The out-of-plane deformation shown in Figure 12, bottom, is mainly induced due to the transverse Poisson's effect, as the layup is symmetric and there is no bending-extension coupling under tensile loading. This transverse deformation will be neglected if the transverse Poisson's ratio ν_{13} and ν_{23} is not introduced into the PD model.

4.3. *Open-hole strength prediction of fiber-reinforced composite laminates.* Three different experiments for open-hole tensile strength of fiber-reinforced composite laminates from the literature are simulated by the present OSB PD composite model. The specimen schematic is shown in Figure 13,
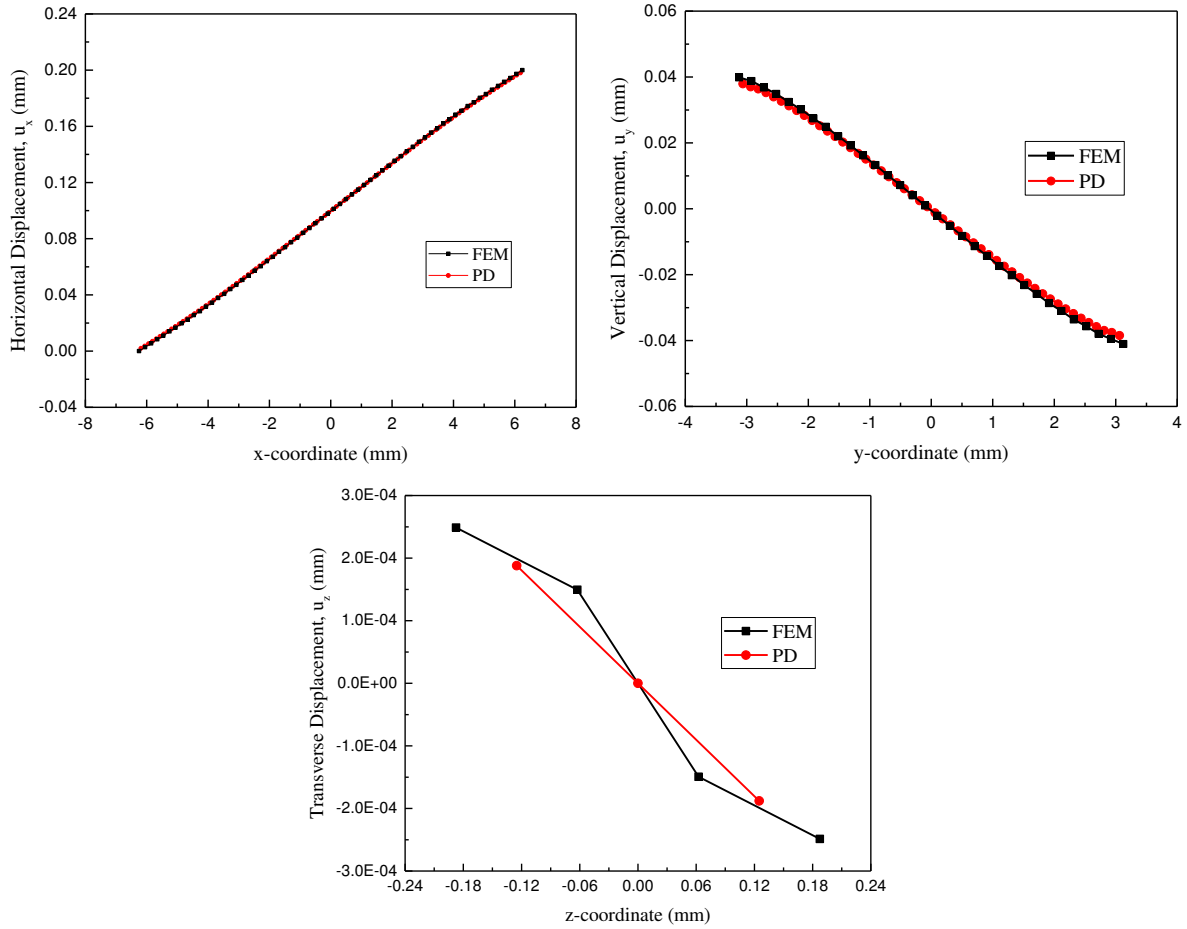
Figure 7. Comparison of the deformation of a composite laminated plate [45/0/45] under tensile loading. Left: along x-axis for midply ($y = 0$, $z = 0$). Right: along y-axis for midply ($x = 0$, $z = 0$). Bottom: along z-axis ($x = 0$, $y = 0$).
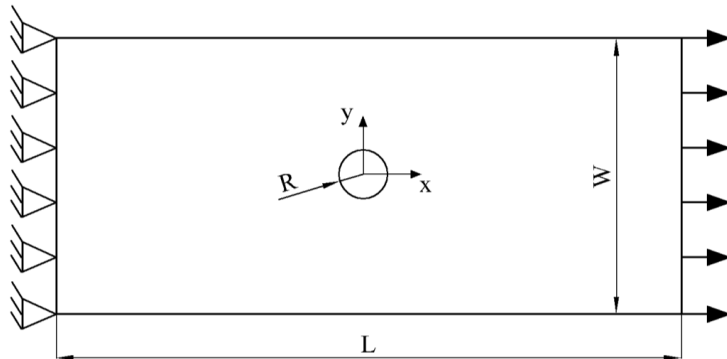

Figure 8. Composite laminated plate [45/0/45] with open-hole under tensile loading.
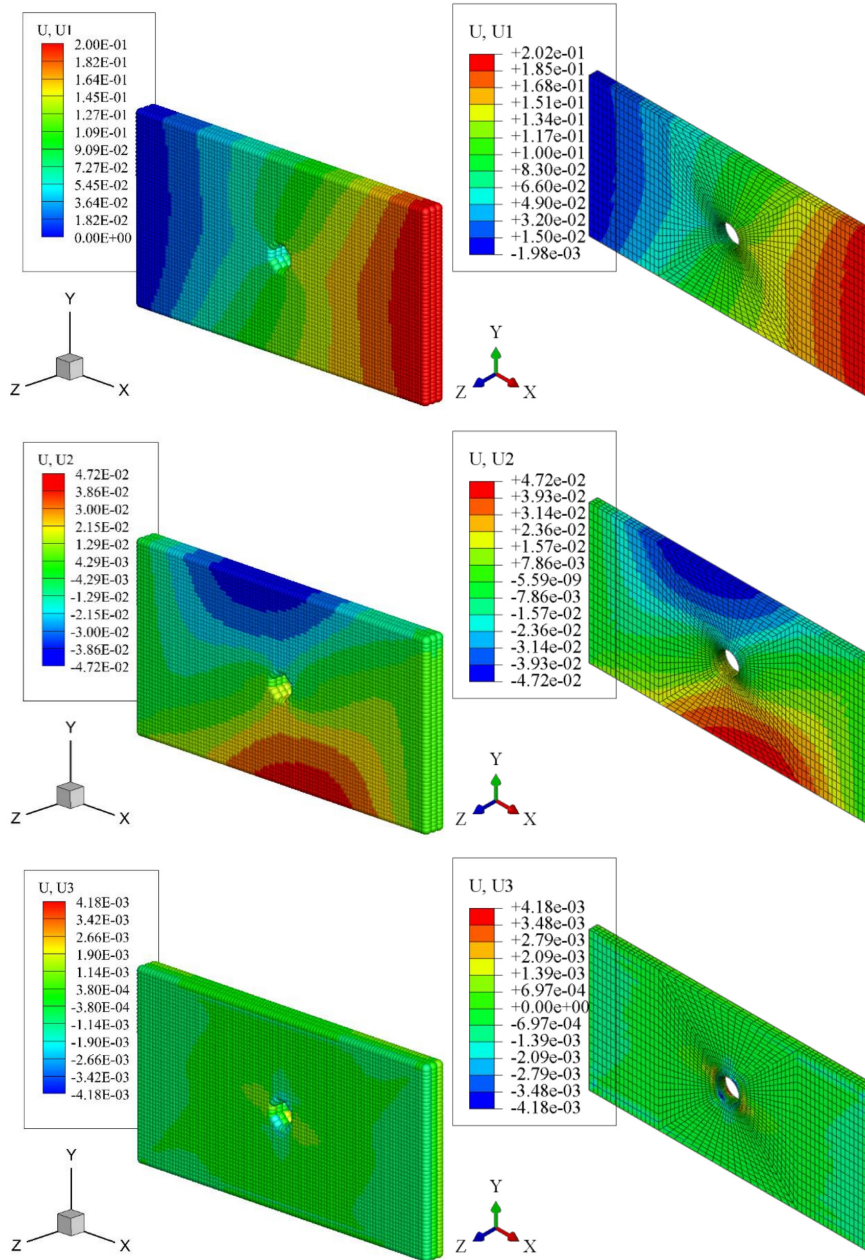
Figure 9. Comparison of the deformation of composite laminated plate [45/0/45] with open-hole (mm). Left: PD. Right: FEM.

bottom. These experiments are renamed in the present paper as specimen A1, A2, and A3. The specimen configurations are shown in Table 1. The material properties of IM7/977-3 and IM7/8552 are shown in Table 2 and Table 3, respectively.
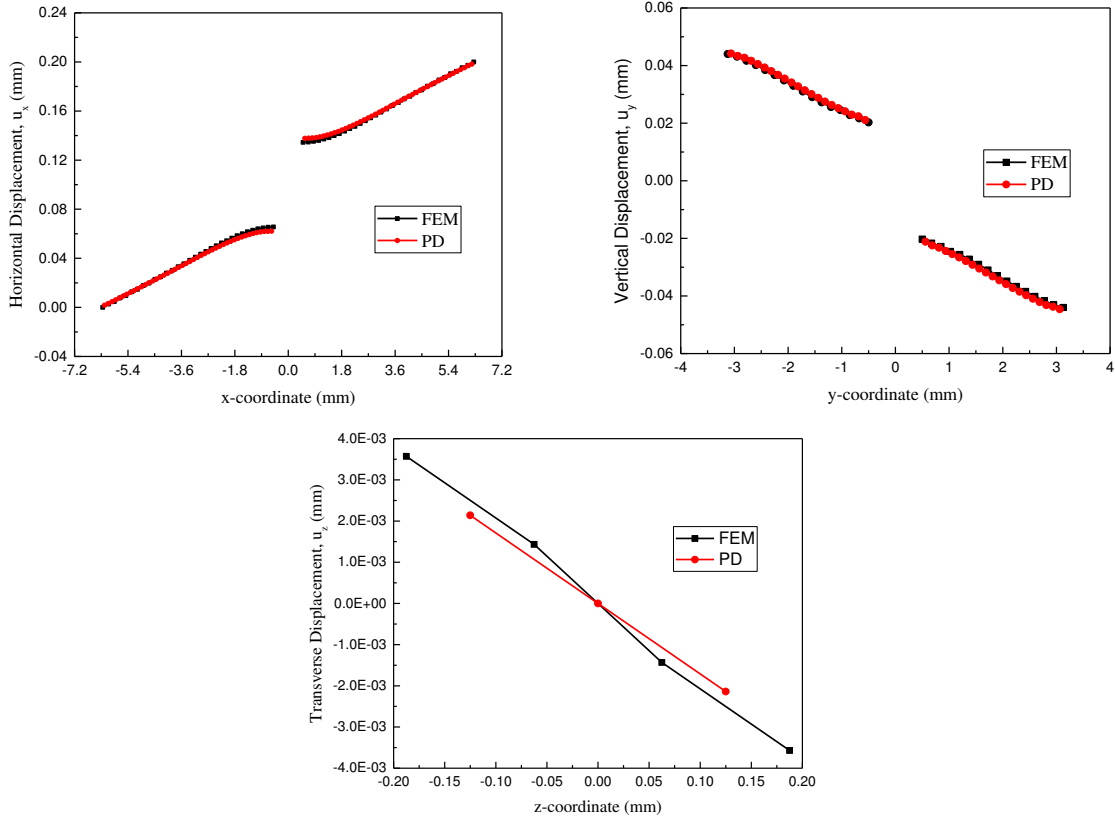
Figure 10. Comparison of the deformation of a composite laminated plate [45/0/45] with an open-hole. Left: along x-axis for midply ($y = 0$, $z = 0$). Right: along y-axis for midply ($x = 0$, $z = 0$). Bottom: along z-direction at the hole edge in the 45° direction ($x = \sqrt{2}R/2$, $y = \sqrt{2}R/2$).

specimen	material system	L	W	D	thickness	layup	h/ply
A1	IM7/977-3	138.43	38.1	6.35	2	$[0/45/90/-45]_{2S}$	0.125
A2	IM7/8552	64	16	3.175	1	$[90/45/0/-45]_S$	0.125
A3	IM7/8552	64	16	3.175	2	$[90_2/45_2/0_2/-45_2]_S$	0.125

Table 1. Specimen configuration of composite laminates with an open-hole: data for A1 are from [Hu and Madenci 2016], whereas data for A2 and A3 are from [Hallett et al. 2007]. All dimensions are in units of mm.

E_1 (GPa)	E_2 (GPa)	G_{12} (GPa)	ν_{12}	X^T (MPa)	X^C (MPa)	Y^T (MPa)	Y^C (MPa)
164.3	8.977	5.02	0.32	2905	1680	100	247

Table 2. Material properties of IM7/977-3 [Hu and Madenci 2016] ($\rho = 1603 \, \text{kg/m}^3$).
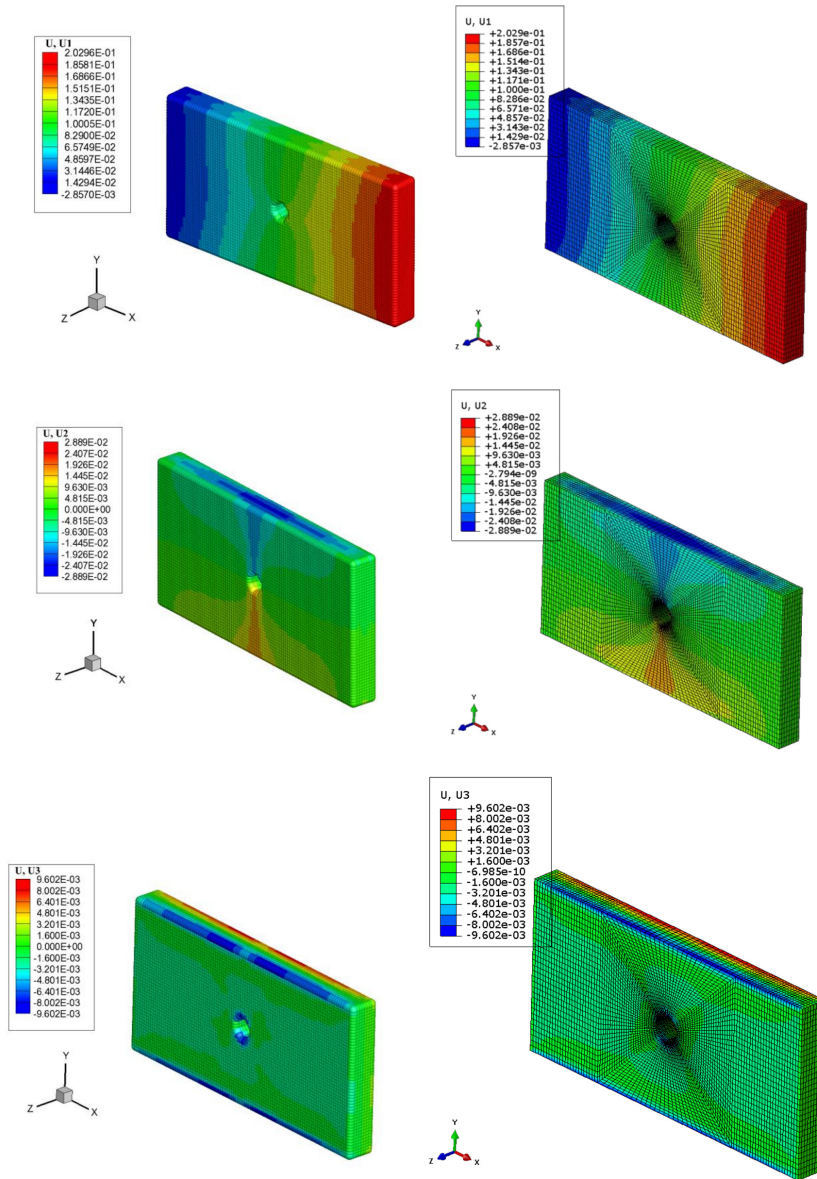
Figure 11. Comparison of the deformation of a composite laminated plate $[90/45/0/-45]_S$ with an open-hole. Left: PD. Right: FEM.

E_1 (GPa)	E_2 (GPa)	G_{12} (GPa)	v_{12}	X^T (MPa)	X^C (MPa)	Y^T (MPa)	Y^C (MPa)
161	11.38	5.17	0.32	2905	1680	100	247

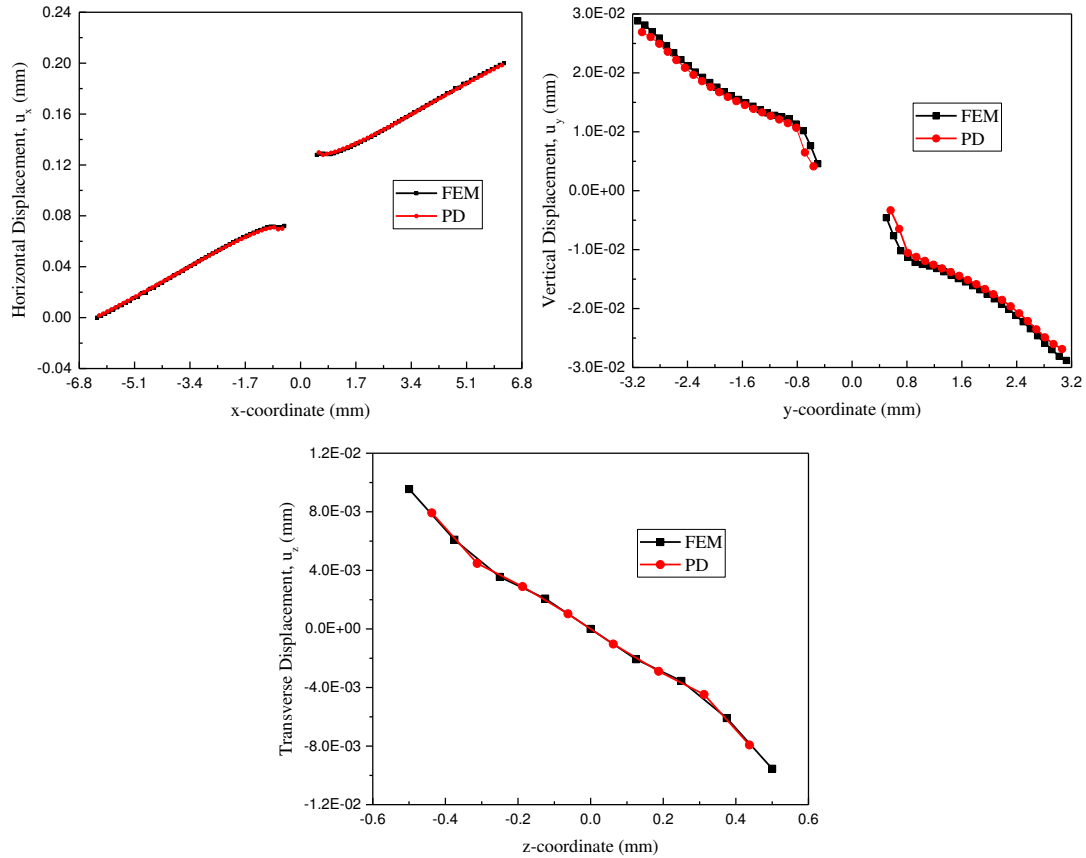**Table 3.** Material properties of IM7/8552 [Camanho and Lambert 2006; Hallett et al. 2007].

Figure 12. Comparison of the deformation of a composite laminated plate $[90/45/0/-45]_S$ with an open-hole. Left: along x-axis for midply ($y = 0$, $z = 0$). Right: along y-axis for midply ($x = 0$, $z = 0$). Bottom: along z direction at the hole edge in the 90° direction ($x = 0$, $y = R$).
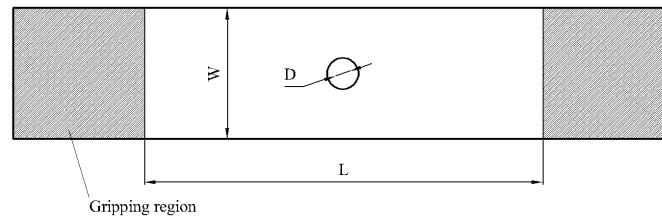

Figure 13. Schematic of open-hole tensile test specimen.

To further the verification of the deformation, the displacement field of specimen A1, with layup $[0/45/90/-45]_{2S}$, is compared with FEM results. Tensile loading of 0.5 mm at the right end of the specimen is applied. The deformation contour is shown in Figure 14, and the variation of the in-plane and out-of-plane displacement in three directions are presented in Figure 16. The vertical and transverse
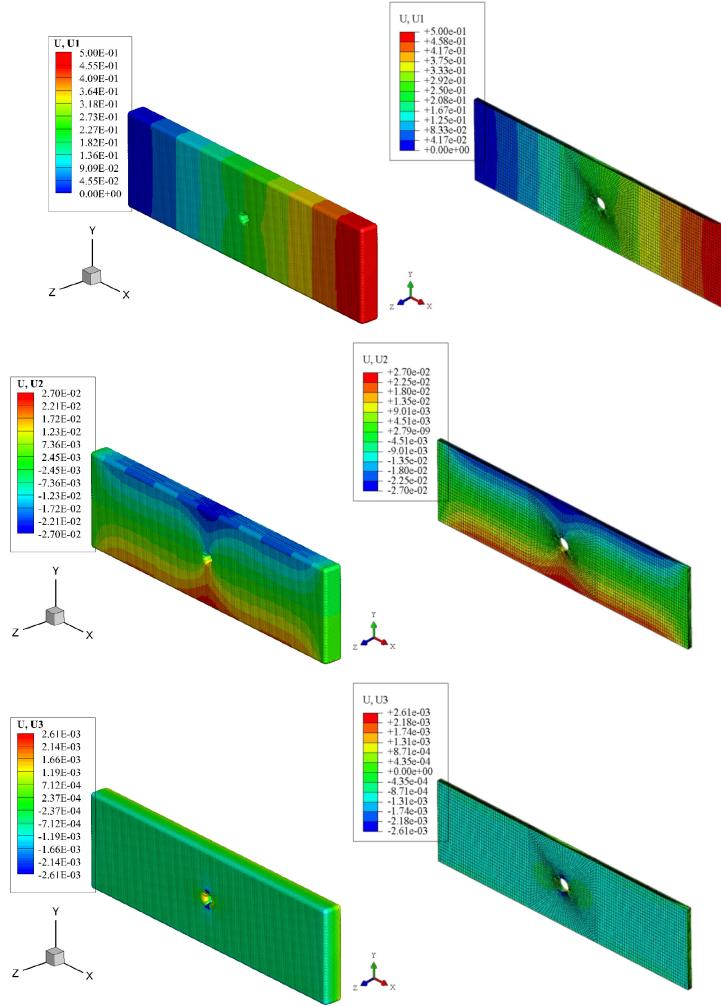
Figure 14. Comparison of the deformation of $[0/45/90/-45]_{2S}$ open-hole composite laminate under tensile loading in x-direction. Left: PD. Right: FEM.

deformation results in Figure 16, right, and Figure 16, bottom, are not as good as the results in Figure 12, right, and Figure 12, bottom. This is mainly due to the usage of an uneven mesh for in-plane and out-of-plane material points. For this specimen A1, $dx \approx 5h$. As using the uneven mesh largely increases the computational efficiency, this slight mismatch between the PD results and FEM results is acceptable. The transverse deformation contour around the hole is also presented in Figure 15. It is interesting to find that for the top surface of the laminate $[0/45/90/-45]_{2S}$, the transverse displacement u_z in the $0°$ direction along the hole edge is positive, while the transverse Poisson's ratio tends to induce a negative displacement for the top surface. It is not possible to capture this phenomenon if the transverse Poisson's ratios ν_{13} and ν_{23} are not introduced into the PD model.

Open-hole tensile strength prediction results and mesh conditions are shown in Table 4. "Uneven spherical horizon" is adopted as $dx > h$, and the horizon $\delta = 3dx$. It can be seen from the table that the
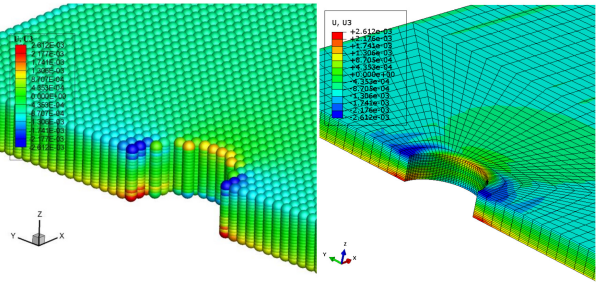
Figure 15. Comparison of the deformation of $[0/45/90/-45]_{2S}$ open-hole composite laminate under tensile loading in x-direction, transverse displacement field around the hole. Left: PD. Right: FEM.
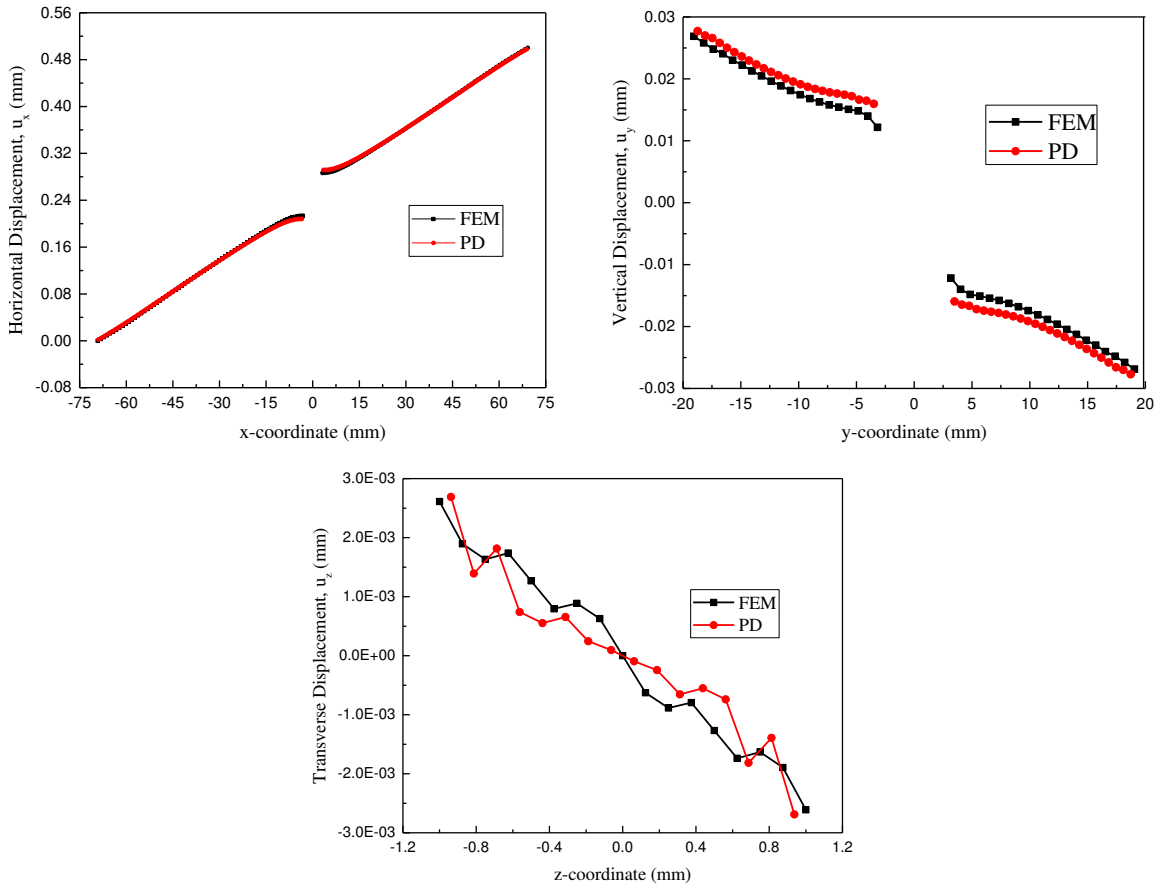

Figure 16. Comparison of the deformation of $[0/45/90/-45]_{2S}$ open-hole composite laminate under tensile loading in x-direction. Left: along x-axis for midply ($y = 0$, $z = 0$). Right: along y-axis for midply ($x = 0$, $z = 0$). Bottom: along z-direction at the hole edge in the $90°$ direction ($x = 0$, $y = R$).

Figure 17. Damage patterns at final failure in each ply of $[0/45/90/-45]_{2S}$ open-hole composite laminate under tensile loading in x-direction.

Figure 18. Displacement field in x-direction u (mm) at final failure of $[0/45/90/-45]_{2S}$ open-hole composite laminate under tensile loading in x-direction.

strength prediction results simulated by the preset OSB PD composite model fit the experimental results well. Damage patterns and failure modes of these specimens are presented in Figures 17–22. Three typical damage modes, fiber breakage, matrix cracking, and delamination, are calculated according to (40). These damage patterns illustrated in Figures 17, 19, and 21 represent a square area around the open-hole of each ply, and the dimension of the square equals the width of the specimen. Final failure modes of the specimens are characterized by the final displacement filed in x-direction, as shown in Figures 18, 20, and 22.
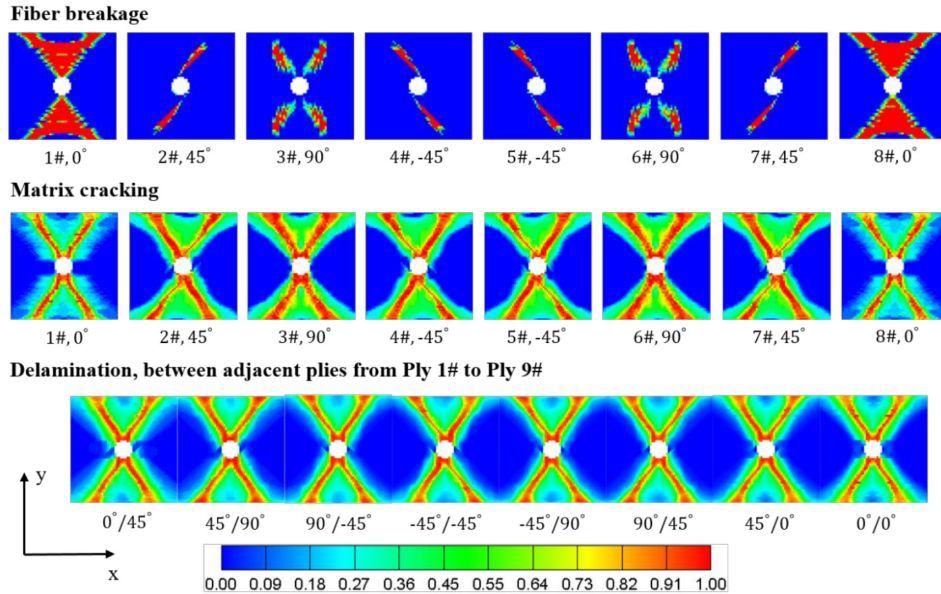
Figure 19. Damage patterns at final failure in each ply of $[90/45/0/-45]_S$ open-hole composite laminate under tensile loading in x-direction.
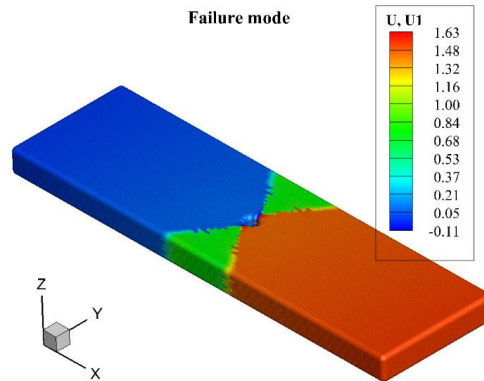

Figure 20. Displacement field in x-direction u (mm) at final failure of $[90/45/0/-45]_S$ open-hole composite laminate under tensile loading in x-direction.

For the open-hole composite laminate specimen A1, with layup $[0/45/90/-45]_{2S}$, it can be seen from Figure 17 that fiber breakage mainly happens in $0°$ plies, and for the $45°$ and $-45°$ plies, the damage direction is consistent with their fiber direction. Matrix cracking and delamination damage form a cross

Fiber breakage

| 1#, 90° | 2#, 90° | 3#, 45° | 4#, 45° | 5#, 0° | 6#, 0° | 7#, -45° | 8#, -45° |

Matrix cracking

| 1#, 90° | 2#, 90° | 3#, 45° | 4#, 45° | 5#, 0° | 6#, 0° | 7#, -45° | 8#, -45° |

Delamination, between adjacent plies from Ply 1# to Ply 9#

| 90°/90° | 90°/45° | 45°/45° | 45°/0° | 0°/0° | 0/-45° | -45°/-45° | -45°/-45° |

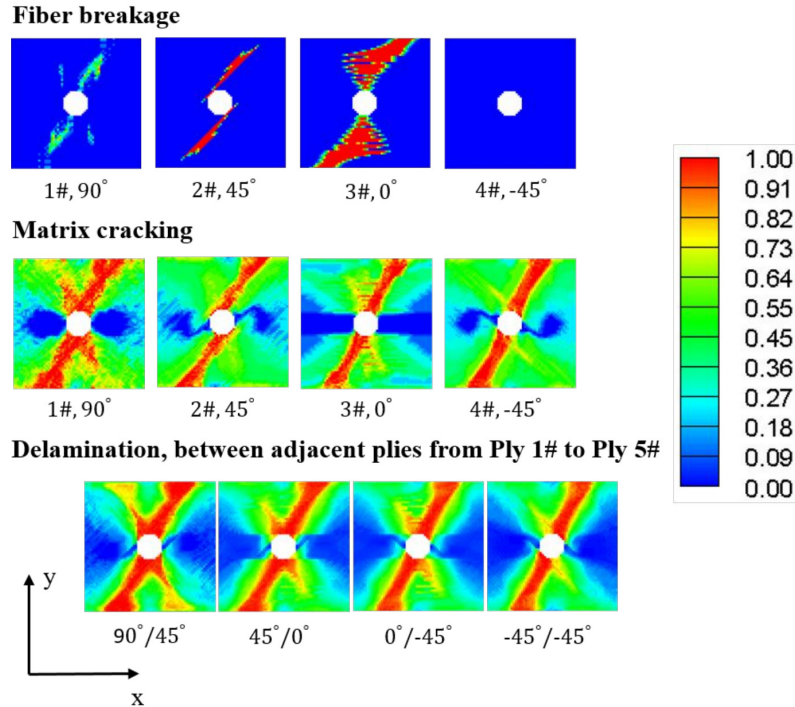0.00 0.09 0.18 0.27 0.36 0.45 0.55 0.64 0.73 0.82 0.91 1.00

Figure 21. Damage patterns at final failure in each ply of $[90_2/45_2/0_2/-45_2]_S$ open-hole composite laminate under tensile loading in x-direction.
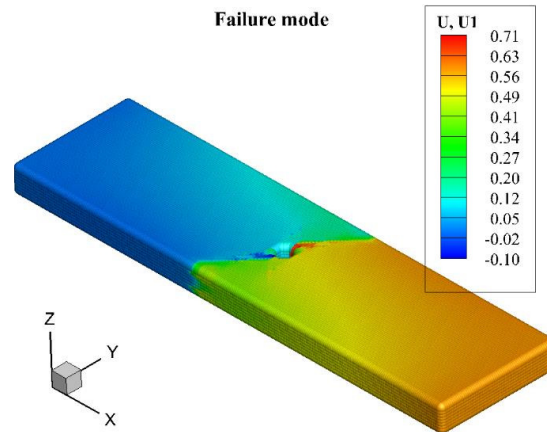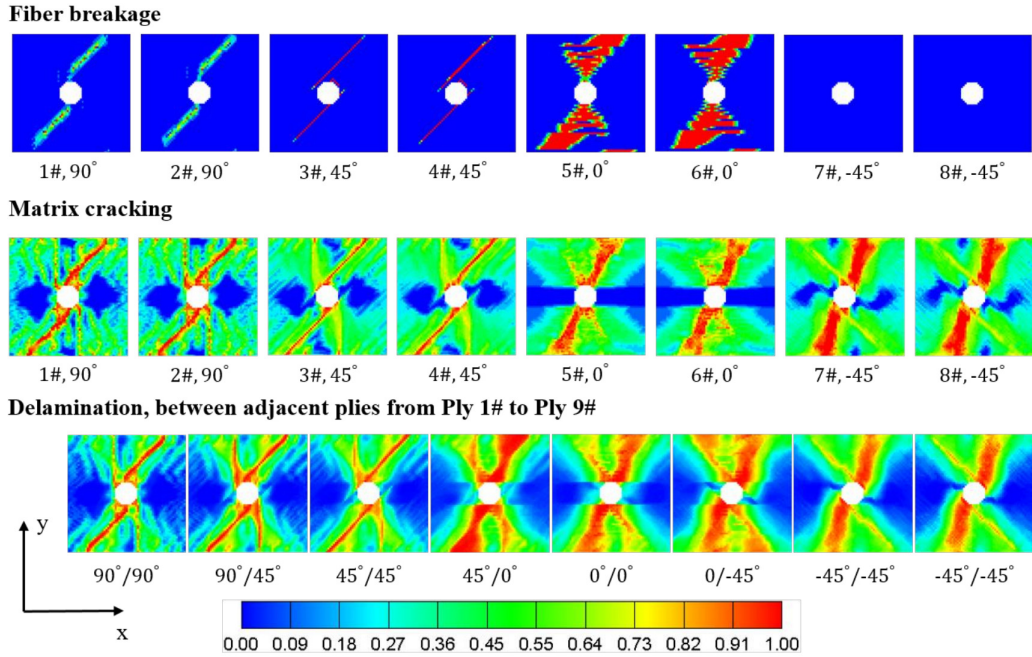
Failure mode
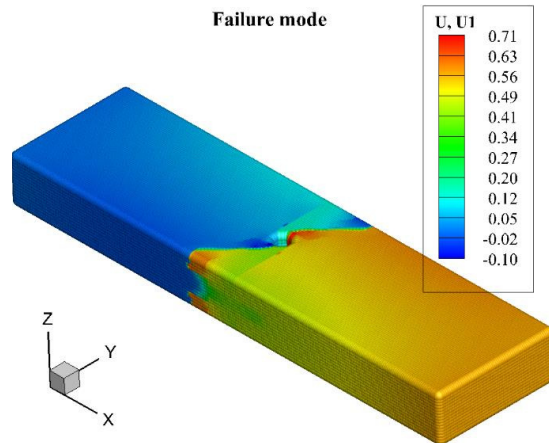
Figure 22. Displacement field in x-direction u (mm) at final failure of $[90_2/45_2/0_2/-45_2]_S$ open-hole composite laminate under tensile loading in x-direction.

$\pm 45°$ area around the open-hole, and matrix cracking in 90° plies are obvious. Figure 18 presents the final failure mode of A1. The specimen fails around the open-hole with cross $\pm 45°$ fracture surface.

For an open-hole composite laminate specimen A2, with layup $[90/45/0/-45]_S$, it can be seen from Figure 19 that similarly to A1, fiber breakage mainly happens in 0° plies, and the damage direction is consistent with their fiber direction for 45° plies. It is interesting that in ply #4 of A2, with fiber direction

specimen	mesh	dx (mm)	h (mm)	experiment (MPa)	PD (MPa)	relative error
A1	$218 \times 60 \times 16$	0.635	0.125	554	590.55	6.6%
A2	$256 \times 64 \times 8$	0.25	0.125	481	462.7	-3.8%
A3	$256 \times 64 \times 16$	0.25	0.125	474	431.25	-9.02%

Table 4. Open-hole tensile strength prediction of fiber-reinforced composite laminates

$-45°$, fiber breakage does not happen. This damage pattern is also detected in A3, as shown in Figure 21; the $-45°$ plies #7 and #8 do not exhibit fiber breakage. Matrix cracking in A2 is severe, and the effect of fiber direction on matrix cracking can be obviously observed by comparing plies #2 and #4 in Figure 19. Delamination between adjacent plies of A2 changes from surface to midplane in the specimen. From Figure 20, we can also observe an obvious 45° fracture surface as the final failure mode of A2.

Specimen A3, with layup $[90_2/45_2/0_2/-45_2]_S$, is directly double the layup of A2. Comparing Figure 19 and Figure 21, we can see that although they both have the same layup proportion, the damage patterns change with an increase in thickness. Comparing the three damage modes of A2 and A3 respectively, we find that the most significant change between A2 and A3 is delamination damage, which indicates that delamination is the most sensitive damage mode to thickness change, and in order to precisely capture the delamination damage, the transverse Poisson's effect should be considered. The final fracture surface of A3 is similar to A2, as shown in Figure 22. From the simulation results of A2 and A3, we can see that the present OSB PD model for composite laminates can capture the effect of thickness on damage patterns, especially for delamination damage.

From the results above, we can conclude that the present OSB PD composite model is validated in open-hole tensile strength prediction of fiber-reinforced composite laminates, and is able to precisely capture the typical damage patterns and failure modes of composite laminates, especially when capturing the effect of thickness on damage patterns.

5. Conclusion

Open-hole strength prediction of fiber-reinforced composite laminates is a fundamental problem in the analysis of composite structures. An ordinary state-based peridynamic (OSB PD) model for open-hole tensile strength prediction is proposed. The transverse Poisson's effect of composites is considered in the present OSB PD composite model, ensuring a precise capture of typical damage patterns and failure modes of composite laminates, especially when capturing the effect of thickness on damage patterns. The out-of-plane bond considers not only the adjacent plies, but also all the plies within the spherical horizon. Although each ply has to be meshed, the in-plane mesh could be much larger than the out-of-plane mesh, forming an "uneven spherical horizon". The validation of the present model is demonstrated by several numerical results. The deformation of a composite laminated plate without and with an open-hole is simulated by both PD and FEM, and the deformation results of the present OSB PD composite model fit the FEM results well. Three different experiments for the open-hole tensile strength of fiber-reinforced composite laminates from the literature are simulated by the present model. By comparing the simulation results with experimental results and discussing the predicted damage patterns and final failure modes, we can conclude that the present OSB PD composite model is validated in open-hole tensile strength

prediction of fiber-reinforced composite laminates, and is able to precisely capture the typical damage patterns and failure modes of composite laminates, especially when capturing the effect of thickness on damage patterns.

Acknowledgments

Appendix

The PD material parameters a, d, b, b_F, and b_T can be derived by comparing the PD strain energy density and the strain energy density of continuum mechanics under simple loading conditions. In the present OSB PD composite model, we derive these parameters by assuming a unidirectional composite laminate under four simple loading conditions:

(1) Transverse pure shear loading on xz-plane (γ_{13}):

$$\gamma_{13} = \zeta, \quad \theta_{(k)}^{CM} = 0, \quad W_{(k)}^{CM} = \tfrac{1}{2}C_{55}\zeta^2, \quad s_{(k)(j)} = \zeta \sin\varphi \cos\varphi \cos\theta.$$

$$W_{(k)}^{(n)} = a\theta_{(k)}^2 + b\sum_{j=1}^{\infty}\delta|\boldsymbol{x}_{(j)} - \boldsymbol{x}_{(k)}|s_{(k)(j)}^2 V_{(j)} + b_F\sum_{j=1}^{J}\delta|\boldsymbol{x}_{(j)}^{(n)} - \boldsymbol{x}_{(k)}^{(n)}|s_{(k)(j)}^{(n)(n)2} V_{(j)}^{(n)}$$

$$+ b_T\sum_{j=1}^{J}\delta|\boldsymbol{x}_{(j)}^{(n)} - \boldsymbol{x}_{(k)}^{(n)}|s_{(k)(j)}^{(n)(n)2} V_{(j)}^{(n)}$$

$$= b\sum_{j=1}^{\infty}\delta|\boldsymbol{x}_{(j)} - \boldsymbol{x}_{(k)}|s_{(k)(j)}^2 V_{(j)} = b\sum_{j=1}^{\infty}\delta\xi(\zeta \sin\varphi \cos\varphi \cos\theta)^2 V_{(j)}$$

$$= \zeta^2 b\delta\int_0^{2\pi}\int_0^{\pi}\int_0^{\delta}\xi \sin^2\varphi \cos^2\varphi \cos^2\theta\, \xi^2 \sin\varphi\, dr\, d\varphi\, d\theta$$

$$= \zeta^2 b\delta\int_0^{2\pi}\cos^2\theta\, d\theta\int_0^{\pi}\sin^3\varphi \cos^2\varphi\, d\varphi\int_0^{\delta}\xi^3\, dr.$$

$$\int_0^{2\pi}\cos^2\theta\, d\theta = \pi, \quad \int_0^{\pi}\sin^3\varphi \cos^2\varphi\, d\varphi = \tfrac{4}{15}, \quad \int_0^{\delta}\xi^3\, dr = \tfrac{1}{4}\delta^4.$$

$$W_{(k)}^{(n)} = \zeta^2 b\delta\pi \times \tfrac{4}{15} \times \tfrac{1}{4}\delta^4 = \zeta^2 b\frac{\pi^2}{15}\delta^5.$$

$$b = \frac{1/2\, C_{55}\zeta^2}{\sum_{j=1}^{\infty}\delta|\boldsymbol{x}_{(j)} - \boldsymbol{x}_{(k)}|s_{(k)(j)}^2 V_{(j)}} = \frac{1/2\, C_{55}\zeta^2}{\zeta^2\pi/15\,\delta^5} = \frac{15C_{55}}{2\pi\,\delta^5}. \tag{A.1}$$

(2) Transverse tensile loading (ε_{33}):

$$\varepsilon_{33} = \zeta, \quad \theta_{(k)}^{CM} = \zeta, \quad W_{(k)}^{CM} = \tfrac{1}{2}C_{33}\zeta^2, \quad s_{(k)(j)} = \zeta \cos^2\varphi.$$

$$\theta_{(k)} = d\sum_{j=1}^{\infty}\delta s_{(k)(j)}\Lambda_{(k)(j)}V_{(j)} = d\sum_{j=1}^{\infty}\delta\zeta\cos^2\varphi V_{(j)} = \zeta d\delta\int_0^{2\pi}\int_0^{\pi}\int_0^{\delta}\cos^2\varphi\,\xi^2\sin\varphi\,\mathrm{d}r\,\mathrm{d}\varphi\,\mathrm{d}\theta$$

$$= \zeta\,\mathrm{d}\delta\int_0^{2\pi}\mathrm{d}\theta\int_0^{\pi}\cos^2\varphi\sin\varphi\,\mathrm{d}\varphi\int_0^{\delta}\xi^2\,\mathrm{d}r.$$

$$\int_0^{\pi}\cos^2\varphi\sin\varphi\,\mathrm{d}\varphi = \tfrac{2}{3}, \quad \theta_{(k)} = \zeta\mathrm{d}\delta 2\pi\times\tfrac{2}{3}\times\tfrac{1}{3}\delta^3 = \zeta d\tfrac{4}{9}\pi\delta^4.$$

$$d = \frac{\zeta}{\sum_{j=1}^{\infty}\delta s_{(k)(j)}\Lambda_{(k)(j)}V_{(j)}} = \frac{\zeta}{\zeta\frac{4}{9}\pi\delta^4} = \frac{9}{4\pi\delta^4}. \tag{A.2}$$

$$W_{(k)}^{(n)} = a\theta_{(k)}^2 + b\sum_{j=1}^{\infty}\delta|\boldsymbol{x}_{(j)} - \boldsymbol{x}_{(k)}|s_{(k)(j)}^2 V_{(j)} + b_F\sum_{j=1}^{J}\delta|\boldsymbol{x}_{(j)}^{(n)} - \boldsymbol{x}_{(k)}^{(n)}|s_{(k)(j)}^{(n)(n)2}V_{(j)}^{(n)}$$

$$+ b_T\sum_{j=1}^{J}\delta|\boldsymbol{x}_{(j)}^{(n)} - \boldsymbol{x}_{(k)}^{(n)}|s_{(k)(j)}^{(n)(n)2}V_{(j)}^{(n)}$$

$$= a\theta_{(k)}^2 + b\sum_{j=1}^{\infty}\delta|\boldsymbol{x}_{(j)} - \boldsymbol{x}_{(k)}|s_{(k)(j)}^2 V_{(j)} = a\zeta^2 + b\sum_{j=1}^{\infty}\delta\xi(\zeta\cos^2\varphi)^2 V_{(j)}$$

$$= a\zeta^2 + \zeta^2 b\delta\int_0^{2\pi}\int_0^{\pi}\int_0^{\delta}\xi\cos^4\varphi\,\xi^2\sin\varphi\,\mathrm{d}r\,\mathrm{d}\varphi\,\mathrm{d}\theta$$

$$= a\zeta^2 + \zeta^2 b\delta\int_0^{2\pi}\mathrm{d}\theta\int_0^{\pi}\cos^4\varphi\sin\varphi\,\mathrm{d}\varphi\int_0^{\delta}\xi^3\,\mathrm{d}r.$$

$$\int_0^{\pi}\cos^4\varphi\sin\varphi\,\mathrm{d}\varphi = \tfrac{2}{5}.$$

$$W_{(k)}^{(n)} = a\zeta^2 + \zeta^2 b\delta 2\pi\times\tfrac{2}{5}\times\tfrac{1}{4}\delta^4 = a\zeta^2 + \zeta^2 b\tfrac{1}{5}\pi\delta^5 = a\zeta^2 + \zeta^2\frac{15C_{55}}{2\pi\delta^5}\tfrac{1}{5}\pi\delta^5 = a\zeta^2 + \zeta^2\tfrac{3}{2}C_{55}.$$

$$a = \tfrac{1}{2}(C_{33} - 3C_{55}). \tag{A.3}$$

(3) In-plane uniaxial tension in x direction (ε_{11}),

$$\varepsilon_{11} = \zeta, \quad \theta_{(k)}^{CM} = \zeta, \quad W_{(k)}^{CM} = \tfrac{1}{2}C_{11}\zeta^2,$$

$$s_{(k)(j)} = \zeta\sin^2\varphi\cos^2\theta.$$

$$\theta_{(k)} = d\sum_{j=1}^{\infty}\delta s_{(k)(j)}\Lambda_{(k)(j)}V_{(j)} = d\sum_{j=1}^{\infty}\delta\zeta\sin^2\varphi\cos^2\theta V_{(j)}$$

$$= \zeta d\delta\int_0^{2\pi}\int_0^{\pi}\int_0^{\delta}\sin^2\varphi\cos^2\theta\,\xi^2\sin\varphi\,\mathrm{d}r\,\mathrm{d}\varphi\,\mathrm{d}\theta$$

$$= \zeta\,d\delta\int_0^{2\pi}\cos^2\theta\mathrm{d}\theta\int_0^{\pi}\sin^3\varphi\,\mathrm{d}\varphi\int_0^{\delta}\xi^2\,\mathrm{d}r.$$

$$\int_0^{2\pi} \cos^2\theta \, d\theta = \pi, \quad \int_0^{\pi} \sin^3\varphi \, d\varphi = \tfrac{4}{3}.$$

$$\theta_{(k)} = \zeta \, d\delta \int_0^{2\pi} \cos^2\theta \, d\theta \int_0^{\pi} \sin^3\varphi \, d\varphi \int_0^{\delta} \xi^2 \, dr = \zeta d\delta\pi \times \tfrac{4}{3} \times \tfrac{1}{3}\delta^3 = \zeta d\tfrac{4}{9}\pi\delta^4.$$

$$d = \frac{\zeta}{\sum_{j=1}^{\infty} \delta s_{(k)(j)} \Lambda_{(k)(j)} V_{(j)}} = \frac{\zeta}{\zeta \, 4/9 \, \pi\delta^4} = \frac{9}{4\pi\delta^4},$$

$$W_{(k)}^{(n)} = a\theta_{(k)}^2 + b\sum_{j=1}^{\infty} \delta|\boldsymbol{x}_{(j)} - \boldsymbol{x}_{(k)}| s_{(k)(j)}^2 V_{(j)} + b_F \sum_{j=1}^{J} \delta|\boldsymbol{x}_{(j)}^{(n)} - \boldsymbol{x}_{(k)}^{(n)}| s_{(k)(j)}^{(n)(n)2} V_{(j)}^{(n)}$$

$$+ b_T \sum_{j=1}^{J} \delta|\boldsymbol{x}_{(j)}^{(n)} - \boldsymbol{x}_{(k)}^{(n)}| s_{(k)(j)}^{(n)(n)2} V_{(j)}^{(n)}$$

$$= a\zeta^2 + b\sum_{j=1}^{\infty} \delta\xi(\zeta \, \sin^2\varphi \, \cos^2\theta)^2 V_{(j)} + b_F \sum_{j=1}^{J} \delta|\boldsymbol{x}_{(j)}^{(n)} - \boldsymbol{x}_{(k)}^{(n)}|(\zeta \, \cos^2\theta)^2 V_{(j)}^{(n)}$$

$$= a\zeta^2 + \zeta^2 b\delta \int_0^{2\pi} \int_0^{\pi} \int_0^{\delta} \xi \, \sin^4\varphi \, \cos^4\theta \, \xi^2 \, \sin\varphi \, dr \, d\varphi \, d\theta + \zeta^2 b_F \delta \sum_{j=1}^{J} |\boldsymbol{x}_{(j)}^{(n)} - \boldsymbol{x}_{(k)}^{(n)}| V_{(j)}^{(n)}$$

$$= a\zeta^2 + \zeta^2 b\delta \int_0^{2\pi} \cos^4\theta \, d\theta \int_0^{\pi} \sin^5\varphi \, d\varphi \int_0^{\delta} \xi^3 \, dr + \zeta^2 b_F \delta \sum_{j=1}^{J} |\boldsymbol{x}_{(j)}^{(n)} - \boldsymbol{x}_{(k)}^{(n)}| V_{(j)}^{(n)}.$$

$$\int_0^{2\pi} \cos^4\theta \, d\theta = \tfrac{3}{4}\pi, \quad \int_0^{\pi} \sin^5\varphi \, d\varphi = \tfrac{16}{15}.$$

$$W_{(k)}^{(n)} = a\zeta^2 + \zeta^2 b\delta \int_0^{2\pi} \cos^4\theta \, d\theta \int_0^{\pi} \sin^5\varphi \, d\varphi \int_0^{\delta} \xi^3 \, dr + \zeta^2 b_F \delta \sum_{j=1}^{J} |\boldsymbol{x}_{(j)}^{(n)} - \boldsymbol{x}_{(k)}^{(n)}| V_{(j)}^{(n)}$$

$$= a\zeta^2 + \zeta^2 b\delta \times \tfrac{3}{4}\pi \times \tfrac{16}{15} \times \tfrac{1}{4}\delta^4 + \zeta^2 b_F \delta \sum_{j=1}^{J} |\boldsymbol{x}_{(j)}^{(n)} - \boldsymbol{x}_{(k)}^{(n)}| V_{(j)}^{(n)}$$

$$= a\zeta^2 + \zeta^2 b\frac{\pi}{5}\delta^5 + \zeta^2 b_F \delta \sum_{j=1}^{J} |\boldsymbol{x}_{(j)}^{(n)} - \boldsymbol{x}_{(k)}^{(n)}| V_{(j)}^{(n)}$$

$$a + b\frac{\pi}{5}\delta^5 + b_F \delta \sum_{j=1}^{J} |\boldsymbol{x}_{(j)}^{(n)} - \boldsymbol{x}_{(k)}^{(n)}| V_{(j)}^{(n)} = \tfrac{1}{2}C_{11}. \tag{A.4}$$

Substituting a and b from (A.3) and (A.1), (A.4) becomes

$$\tfrac{1}{2}(C_{33} - 3C_{55}) + \frac{15C_{55}}{2\pi\delta^5} \times \frac{\pi}{5}\delta^5 + b_F \delta \sum_{j=1}^{J} |\boldsymbol{x}_{(j)}^{(n)} - \boldsymbol{x}_{(k)}^{(n)}| V_{(j)}^{(n)} = \tfrac{1}{2}C_{11},$$

$$\tfrac{1}{2}(C_{11} - 3C_{55}) + \tfrac{3}{2}C_{55} + b_F \delta \sum_{j=1}^{J} |\boldsymbol{x}_{(j)}^{(n)} - \boldsymbol{x}_{(k)}^{(n)}| V_{(j)}^{(n)} = \tfrac{1}{2}C_{11},$$

$$b_F = \frac{1/2\,(C_{11} - C_{33})}{\delta \sum_{j=1}^{J} |\boldsymbol{x}_{(j)}^{(n)} - \boldsymbol{x}_{(k)}^{(n)}| V_{(j)}^{(n)}}. \tag{A.5}$$

(4) In-plane uniaxial tension in y direction (ε_{22}):

$$\varepsilon_{22} = \zeta, \quad \theta_{(k)}^{CM} = \zeta, \quad W_{(k)}^{CM} = \tfrac{1}{2} C_{22} \zeta^2,$$

$$s_{(k)(j)} = \zeta \sin^2\varphi \sin^2\theta.$$

$$\theta_{(k)} = d \sum_{j=1}^{\infty} \delta s_{(k)(j)} \Lambda_{(k)(j)} V_{(j)} = d \sum_{j=1}^{\infty} \delta \zeta \sin^2\varphi \sin^2\theta \, V_{(j)}$$

$$= \zeta \, d\delta \int_0^{2\pi} \int_0^{\pi} \int_0^{\delta} \sin^2\varphi \sin^2\theta \, \xi^2 \sin\varphi \, dr \, d\varphi \, d\theta$$

$$= \zeta \, d\delta \int_0^{2\pi} \sin^2\theta \, d\theta \int_0^{\pi} \sin^3\varphi \, d\varphi \int_0^{\delta} \xi^2 \, dr.$$

$$\int_0^{2\pi} \sin^2\theta \, d\theta = \pi, \quad \int_0^{\pi} \sin^3\varphi \, d\varphi = \tfrac{4}{3}.$$

$$\theta_{(k)} = \zeta \, d\delta \int_0^{2\pi} \sin^2\theta \, d\theta \int_0^{\pi} \sin^3\varphi \, d\varphi \int_0^{\delta} \xi^2 \, dr = \zeta \, d\delta\pi \times \tfrac{4}{3} \times \tfrac{1}{3}\delta^3 = \zeta \, d\tfrac{4}{9}\pi\delta^4.$$

$$d = \frac{\zeta}{\sum_{j=1}^{\infty} \delta s_{(k)(j)} \Lambda_{(k)(j)} V_{(j)}} = \frac{\zeta}{\zeta \frac{4}{9}\pi\delta^4} = \frac{9}{4\pi\delta^4}.$$

$$W_{(k)}^{(n)} = a\theta_{(k)}^2 + b \sum_{j=1}^{\infty} \delta|\boldsymbol{x}_{(j)} - \boldsymbol{x}_{(k)}| s_{(k)(j)}^2 V_{(j)} + b_F \sum_{j=1}^{J} \delta|\boldsymbol{x}_{(j)}^{(n)} - \boldsymbol{x}_{(k)}^{(n)}| s_{(k)(j)}^{(n)(n)2} V_{(j)}^{(n)}$$

$$+ b_T \sum_{j=1}^{J} \delta|\boldsymbol{x}_{(j)}^{(n)} - \boldsymbol{x}_{(k)}^{(n)}| s_{(k)(j)}^{(n)(n)2} V_{(j)}^{(n)}$$

$$= a\zeta^2 + b \sum_{j=1}^{\infty} \delta\xi(\zeta \sin^2\varphi \sin^2\theta)^2 V_{(j)} + b_T \sum_{j=1}^{J} \delta|\boldsymbol{x}_{(j)}^{(n)} - \boldsymbol{x}_{(k)}^{(n)}|(\zeta \sin^2\theta)^2 V_{(j)}^{(n)}$$

$$= a\zeta^2 + \zeta^2 b\delta \int_0^{2\pi} \int_0^{\pi} \int_0^{\delta} \xi \sin^4\varphi \sin^4\theta \, \xi^2 \sin\varphi \, dr \, d\varphi \, d\theta + \zeta^2 b_T \delta \sum_{j=1}^{J} |\boldsymbol{x}_{(j)}^{(n)} - \boldsymbol{x}_{(k)}^{(n)}| V_{(j)}^{(n)}$$

$$= a\zeta^2 + \zeta^2 b\delta \int_0^{2\pi} \sin^4\theta \, d\theta \int_0^{\pi} \sin^5\varphi \, d\varphi \int_0^{\delta} \xi^5 \, dr + \zeta^2 b_T \delta \sum_{j=1}^{J} |\boldsymbol{x}_{(j)}^{(n)} - \boldsymbol{x}_{(k)}^{(n)}| V_{(j)}^{(n)}.$$

$$\int_0^{2\pi} \sin^4\theta \, d\theta = \tfrac{3}{4}\pi, \quad \int_0^{\pi} \sin^5\varphi \, d\varphi = \tfrac{16}{15}.$$

$$W_{(k)}^{(n)} = a\zeta^2 + \zeta^2 b\delta \int_0^{2\pi} \sin^4\theta \, d\theta \int_0^{\pi} \sin^5\varphi \, d\varphi \int_0^{\delta} \xi^3 \, dr + \zeta^2 b_T \delta \sum_{j=1}^{J} |\boldsymbol{x}_{(j)}^{(n)} - \boldsymbol{x}_{(k)}^{(n)}| V_{(j)}^{(n)}$$

$$= a\zeta^2 + \zeta^2 b\delta \times \tfrac{3}{4}\pi \times \tfrac{16}{15} \times \tfrac{1}{4}\delta^4 + \zeta^2 b_T \delta \sum_{j=1}^{J} |\boldsymbol{x}_{(j)}^{(n)} - \boldsymbol{x}_{(k)}^{(n)}| V_{(j)}^{(n)}$$

$$= a\zeta^2 + \zeta^2 b\frac{\pi}{5}\delta^5 + \zeta^2 b_T \delta \sum_{j=1}^{J} |\boldsymbol{x}_{(j)}^{(n)} - \boldsymbol{x}_{(k)}^{(n)}| V_{(j)}^{(n)}.$$

$$a + b\frac{\pi}{5}\delta^5 + b_T \delta \sum_{j=1}^{J} |\boldsymbol{x}_{(j)}^{(n)} - \boldsymbol{x}_{(k)}^{(n)}| V_{(j)}^{(n)} = \tfrac{1}{2} C_{22}. \tag{A.6}$$

Substituting a and b from (A.3) and (A.1), (A.6) becomes

$$\tfrac{1}{2}(C_{33} - 3C_{55}) + \frac{15 C_{55}}{2\pi \delta^5} \times \frac{\pi}{5}\delta^5 + b_T \delta \sum_{j=1}^{J} |\boldsymbol{x}_{(j)}^{(n)} - \boldsymbol{x}_{(k)}^{(n)}| V_{(j)}^{(n)} = \tfrac{1}{2} C_{22},$$

$$\tfrac{1}{2}(C_{33} - 3C_{55}) + \tfrac{3}{2} C_{55} + b_T \delta \sum_{j=1}^{J} |\boldsymbol{x}_{(j)}^{(n)} - \boldsymbol{x}_{(k)}^{(n)}| V_{(j)}^{(n)} = \tfrac{1}{2} C_{22},$$

$$b_T = \frac{1/2\,(C_{22} - C_{33})}{\delta \sum_{j=1}^{J} |\boldsymbol{x}_{(j)}^{(n)} - \boldsymbol{x}_{(k)}^{(n)}| V_{(j)}^{(n)}}. \tag{A.7}$$

References

[Aidi and Case 2015] B. Aidi and S. W. Case, "Experimental and numerical analysis of notched composites under tension loading", *Appl. Compos. Mater.* **22**:6 (2015), 837–855.

[Askari et al. 2006] E. Askari, J. Xu, and S. A. Silling, "Peridynamic analysis of damage and failure in composites", in *44th AIAA aerospace sciences meeting and exhibition* (Reno), 2006.

[ASTM 2011] "Standard test method for open-hole tensile strength of polymer matrix composite laminates", standard, American Society for Testing and Materials (ASTM) International, West Conshohocken, PA, 2011.

[Bao and Liu 2016] H. Bao and G. Liu, "Progressive failure analysis on scaled open-hole tensile composite laminates", *Compos. Struct.* **150** (2016), 173–180.

[Bartan et al. 2016] B. Bartan, B. Acar, and A. Kayran, "Three-dimensional delamination analysis in composite open hole tensile specimens with cohesive zone method", in *57th AIAA/ASCE/AHS/ASC structures, structural dynamics, and materials conference*, 2016.

[Camanho and Lambert 2006] P. P. Camanho and M. Lambert, "A design methodology for mechanically fastened joints in laminated composite materials", *Compos. Sci. Technol.* **66**:15 (2006), 3004–3020.

[Camanho et al. 2007] P. P. Camanho, P. Maimí, and C. G. Dávila, "Prediction of size effects in notched laminates using continuum damage mechanics", *Compos. Sci. Technol.* **67**:13 (2007), 2715–2727.

[Chen et al. 2013] B. Y. Chen, T. E. Tay, P. M. Baiz, and S. T. Pinho, "Numerical analysis of size effects on open-hole tensile composite laminates", *Compos. A Appl. Sci. Manuf.* **47** (2013), 52–62.

[Colavito 2013] K. Colavito, *Peridynamics for failure and residual strength prediction of fiber-reinforced composites*, electronic dissertation, University of Arizona, 2013, available at http://arizona.openrepository.com/arizona/handle/10150/311300.

[Colavito and Barut 2013] K. Colavito and A. E. M. Barut, "Residual strength of composite laminates with a hole by using peridynamic theory", in *54th AIAA/ASME/ASCE/AHS/ASC structures, structural dynamics, and materials conference* (Boston), 2013.

[Diyaroglu et al. 2016] C. Diyaroglu, E. Oterkus, E. Madenci, T. Rabczuk, and A. Siddiq, "Peridynamic modeling of composite laminates under explosive loading", *Compos. Struct.* **144** (2016), 14–23.

[Hallett et al. 2007] S. Hallett, W.-G. Jiang, and M. Wisnom, "The effect of stacking sequence on thickness scaling of tests on open hole tensile composite specimens", in *48th AIAA/ASME/ASCE/AHS/ASC structures, structural dynamics, and materials conference* (Honolulu), 2007.

[Hallett et al. 2009] S. R. Hallett, B. G. Green, W. G. Jiang, and M. R. Wisnom, "An experimental and numerical investigation into the damage mechanisms in notched composites", *Compos. A Appl. Sci. Manuf.* **40**:5 (2009), 613–624.

[Hu and Madenci 2016] Y. L. Hu and E. Madenci, "Bond-based peridynamic modeling of composite laminates with arbitrary fiber orientation and stacking sequence", *Compos. Struct.* **153** (2016), 139–175.

[Hu et al. 2011] W. K. Hu, Y. D. Ha, and F. Bobaru, "Modeling dynamic fracture and damage in a fiber-reinforced composite lamina with peridynamics", *Int. J. Multiscale Comput. Eng.* **9**:6 (2011), 707–726.

[Hu et al. 2012] W. K. Hu, Y. D. Ha, and F. Bobaru, "Peridynamic model for dynamic fracture in unidirectional fiber-reinforced composites", *Comput. Methods Appl. Mech. Eng.* **217** (2012), 247–261.

[Hu et al. 2014] Y. L. Hu, Y. Yu, and H. Wang, "Peridynamic analytical method for progressive damage in notched composite laminates", *Compos. Struct.* **108** (2014), 801–810.

[Hu et al. 2015] Y. L. Hu, N. V. De Carvalho, and E. Madenci, "Peridynamic modeling of delamination growth in composite laminates", *Compos. Struct.* **132** (2015), 610–620.

[Hu et al. 2016] Y. L. Hu, E. Madenci, and N. D. Phan, "Peridynamics for predicting tensile and compressive strength of notched composites", in *57th AIAA/ASCE/AHS/ASC structures, structural dynamics, and materials conference* (San Diego), 2016.

[Kilic and Madenci 2010] B. Kilic and E. Madenci, "An adaptive dynamic relaxation method for quasi-static simulations using the peridynamic theory", *Theor. Appl. Fract. Mech.* **53**:3 (2010), 194–204.

[Kilic et al. 2009] B. Kilic, A. Agwai, and E. Madenci, "Peridynamic theory for progressive damage prediction in center-cracked composite laminates", *Compos. Struct.* **90**:2 (2009), 141–151.

[Madenci and Oterkus 2014] E. Madenci and E. Oterkus, *Peridynamic theory and its applications*, Springer, New York, 2014.

[Mohammadi et al. 2017] R. Mohammadi, M. A. Najafabadi, M. Saeedifar, J. Yousefi, and G. Minak, "Correlation of acoustic emission with finite element predicted damages in open-hole tensile laminated composites", *Compos. B Eng.* **108** (2017), 427–435.

[Moure et al. 2016] M. M. Moure, S. K. García-Castillo, S. Sánchez-Sáez, E. Barbero, and E. J. Barbero, "Influence of ply cluster thickness and location on matrix cracking evolution in open-hole composite laminates", *Compos. B Eng.* **95** (2016), 40–47.

[Oterkus and Madenci 2012a] E. Oterkus and E. Madenci, "Peridynamic analysis of fiber-reinforced composite materials", *J. Mech. Mater. Struct.* **7**:1 (2012), 45–84.

[Oterkus and Madenci 2012b] E. Oterkus and E. Madenci, "Peridynamic theory for damage initiation and growth in composite laminate", pp. 355 in *Advances in fracture and damage mechanics X*, vol. 488–489, edited by Z. Tonkovic and M. H. Aliabadi, 2012.

[Oterkus et al. 2010] E. Oterkus, A. Barut, and E. Madenci, "Damage growth prediction from loaded composite fastener holes by using peridynamic theory", in *51st AIAA/ASME/ASCE/AHS/ASC structures, structural dynamics, and materials conference* (Orlando), 2010.

[Oterkus et al. 2012] E. Oterkus, E. Madenci, O. Weckner, S. Silling, P. Bogert, and A. Tessler, "Combined finite element and peridynamic analyses for predicting failure in a stiffened composite curved panel with a central slot", *Compos. Struct.* **94**:3 (2012), 839–850.

[Ruetsch and Fatica 2013] G. Ruetsch and M. Fatica, *CUDA Fortran for scientists and engineers: best practices for efficient CUDA Fortran programming*, Elsevier, Burlington, MA, 2013.

[Silling 2000] S. A. Silling, "Reformulation of elasticity theory for discontinuities and long-range forces", *J. Mech. Phys. Solids* **48**:1 (2000), 175–209.

[Silling and Askari 2005] S. A. Silling and E. Askari, "A meshfree method based on the peridynamic model of solid mechanics", *Comput. Struct.* **83**:17–18 (2005), 1526–1535.

[Silling and Lehoucq 2010] S. A. Silling and R. B. Lehoucq, "Peridynamic theory of solid mechanics", pp. 73–168 in *Advances in applied mechanics*, vol. 44, edited by H. Aref and E. van der Giessen, 2010.

[Silling et al. 2007] S. A. Silling, M. Epton, O. Weckner, J. Xu, and E. Askari, "Peridynamic states and constitutive modeling", *J. Elasticity* **88**:2 (2007), 151–184.

[Su et al. 2015] Z. C. Su, T. E. Tay, M. Ridha, and B. Y. Chen, "Progressive damage modeling of open-hole composite laminates under compression", *Compos. Struct.* **122** (2015), 507–517.

[Sun and Huang 2016] C. Y. Sun and Z. X. Huang, "Peridynamic simulation to impacting damage in composite laminate", *Compos. Struct.* **138** (2016), 335–341.

[US-DoD 2002] *Composite materials handbook*, Army Research Laboratory, Weapons and Materials Research Directorate, 2002.

[Xu et al. 2007] J. F. Xu, A. Askari, O. Weckner, H. Razi, and S. Silling, "Damage and failure analysis of composite laminates under biaxial loads", in *48th AIAA/ASME/ASCE/AHS/ASC structures, structural dynamics, and materials conference* (Honolulu), 2007.

[Xu et al. 2008] J. F. Xu, A. Askari, O. Weckner, and S. Silling, "Peridynamic analysis of impact damage in composite laminates", *J. Aerosp. Eng.* (*ASCE*) **21**:3 (2008), 187–194.

[Yu et al. 2016] Y. Yu, S. S. Liu, S. L. Zhao, and Z. Yu, "The nonlinear inplane behavior and progressive damage modeling for laminate by peridynamics", in *ASME 2016 international mechanical engineering congress and exposition* (Phoenix), 2016.

XIAO-WEI JIANG: jiangxiaowei@sjtu.edu.cn
School of Aeronautics and Astronautics, Shanghai Jiao Tong University, Shanghai, China

HAI WANG: wanghai601@sjtu.edu.cn
School of Aeronautics and Astronautics, Shanghai Jiao Tong University, Shanghai, China